

NASA TECHNICAL NOTE



NASA TN D-5361

NASA TN D-5361

CASE FILE COPY

ANALYSIS OF LATERAL-DIRECTIONAL
STABILITY CHARACTERISTICS OF A
TWIN-JET FIGHTER AIRPLANE
AT HIGH ANGLES OF ATTACK

by Joseph R. Chambers and Ernie L. Anglin

Langley Research Center

Langley Station, Hampton, Va.

1. Report No. NASA TN D-5361	2. Government Accession No.	3. Recipient's Catalog No.	
4. Title and Subtitle ANALYSIS OF LATERAL-DIRECTIONAL STABILITY CHARACTERISTICS OF A TWIN-JET FIGHTER AIRPLANE AT HIGH ANGLES OF ATTACK		5. Report Date August 1969	6. Performing Organization Code
		8. Performing Organization Report No. L-6723	
7. Author(s) Joseph R. Chambers and Ernie L. Anglin		10. Work Unit No. 126-62-01-01-23	
9. Performing Organization Name and Address NASA Langley Research Center Langley Station Hampton, Va. 23365		11. Contract or Grant No.	
		13. Type of Report and Period Covered Technical Note	
12. Sponsoring Agency Name and Address National Aeronautics and Space Administration Washington, D.C. 20546		14. Sponsoring Agency Code	
		15. Supplementary Notes	
16. Abstract An investigation was conducted to determine the factors producing a directional divergence at high angles of attack for a twin-jet swept-wing fighter airplane. The study consisted of static wind-tunnel tests, tuft-flow visualization tests, and calculations of the dynamic lateral-directional stability characteristics of the airplane. Several modifications to the basic configuration were evaluated in an attempt to delay or eliminate the instability.			
17. Key Words Suggested by Author(s) Lateral-directional stability Dynamic stability Stability at high angles of attack		18. Distribution Statement Unclassified - Unlimited	
19. Security Classif. (of this report) Unclassified	20. Security Classif. (of this page) Unclassified	21. No. of Pages 47	22. Price* \$3.00

*For sale by the Clearinghouse for Federal Scientific and Technical Information

Springfield, Virginia 22151

ANALYSIS OF LATERAL-DIRECTIONAL STABILITY CHARACTERISTICS OF A TWIN-JET FIGHTER AIRPLANE AT HIGH ANGLES OF ATTACK

By Joseph R. Chambers and Ernie L. Anglin
Langley Research Center

SUMMARY

An investigation was conducted to determine the factors producing a directional divergence at high angles of attack for a twin-jet swept-wing fighter airplane. The study consisted of static wind-tunnel tests, tuft-flow visualization tests, and calculations of the dynamic lateral-directional stability characteristics of the airplane. Several modifications to the basic configuration were evaluated in an attempt to delay or eliminate the instability.

The results of the investigation indicated that the directional divergence exhibited by the airplane was brought about by a simultaneous loss of directional stability and effective dihedral at high angles of attack. The loss of directional stability resulted from a combination of an adverse sidewash region at the rear of the airplane and a reduced dynamic pressure at the vertical tail location. The adverse sidewash was generated by the wing-fuselage combination and was related to stalling of the leading-wing panel during a sideslip at high angles of attack. The loss of effective dihedral was also attributed to leading-wing-panel stall. The apparent directional divergence was determined to be, in reality, a highly unstable Dutch roll oscillation. The only geometric modification studied that significantly delayed the divergence was wing leading-edge droop.

INTRODUCTION

The National Aeronautics and Space Administration is currently conducting a series of investigations of the poststall characteristics of a high-performance swept-wing fighter airplane. Recently, concern has arisen over the existence of directional divergence (sometimes termed "nose slice") at angles of attack near the stall. Tactical training and air combat maneuver requirements imposed on the airplane have resulted in operational angles of attack near the stall and the associated directional divergence which in turn has produced inadvertent poststall gyrations and spins. Inasmuch as instabilities of this type can seriously limit the maneuvering capability of an airplane, the present investigation was conducted (1) to identify the various factors producing the directional divergence and (2) to define geometric modifications or fixes which might eliminate or postpone the

instability to angles of attack farther removed from the operational flight envelope. The study consisted of static wind-tunnel force tests, flow visualization tests, and calculations of the dynamic lateral-directional stability of the airplane.

SYMBOLS

All aerodynamic data with the exception of lift and drag are presented with respect to a body system of axes. Moment data are presented with respect to a center-of-gravity position of 33 percent of the wing mean aerodynamic chord. Dimensional values herein are given in both U.S. Customary Units and in the International System of Units.

A,B,C,D,E	coefficients of lateral-directional characteristic equation (see appendix A)
b	wing span, ft (m)
\bar{c}	mean aerodynamic chord, ft (m)
\bar{c}_t	mean aerodynamic chord of horizontal tail, ft (m)
C_D	drag coefficient, $F_D/q_\infty S$
C_L	lift coefficient, $F_L/q_\infty S$
C_l	rolling-moment coefficient, $M_X/q_\infty S b$
C_m	pitching-moment coefficient, $M_Y/q_\infty S \bar{c}$
C_n	yawing-moment coefficient, $M_Z/q_\infty S b$
C_Y	side-force coefficient, $F_Y/q_\infty S$
D_b	differential operator, d/ds_b
F_D	drag force, lb (N)
F_L	lift force, lb (N)
F_Y	side force, lb (N)
i_t	horizontal tail deflection (positive when trailing edge is down), deg

I_X	moment of inertia about longitudinal body axis, slug-ft ² (kg-m ²)
I_Y	moment of inertia about lateral body axis, slug-ft ² (kg-m ²)
I_Z	moment of inertia about normal body axis, slug-ft ² (kg-m ²)
I_{XZ}	product of inertia, slug-ft ² (kg-m ²)
k_{X_0}	radius of gyration in roll about principal longitudinal axis, ft (m)
k_{Z_0}	radius of gyration in yaw about principal normal axis, ft (m)
K_{X_0}	nondimensional radius of gyration in roll about principal longitudinal axis, k_{X_0}/b
K_{Z_0}	nondimensional radius of gyration in yaw about principal normal axis, k_{Z_0}/b
l_v	vertical tail length, distance from moment reference center to aerodynamic center of vertical tail measured along fuselage center line, ft (m)
m	airplane mass, slugs (kg)
M	Mach number
M_X	rolling moment, ft-lb (m-N)
M_Y	pitching moment, ft-lb (m-N)
M_Z	yawing moment, ft-lb (m-N)
p	rolling velocity, rad/sec
P	period of oscillation, sec
q_v	effective dynamic pressure at vertical tail location, lb/ft ² (N/m ²)
q_∞	free-stream dynamic pressure, lb/ft ² (N/m ²)
r	yawing velocity, rad/sec

- S wing area, ft² (m²)
- s_b nondimensional time parameter based on wing span, Vt/b
- t time, sec
- t_{1/2} time required for amplitude of oscillation to decrease by a factor of 2, sec
- V velocity, ft/sec (m/sec)
- α angle of attack, deg or rad
- β angle of sideslip, deg or rad
- β₀, φ₀, ψ₀ constants used in solution of characteristic equation
- λ root of lateral-directional characteristic equation

$$A\lambda^4 + B\lambda^3 + C\lambda^2 + D\lambda + E = 0$$
- μ_b lateral-directional relative-density factor, m/ρSb
- ρ mass density of air, slugs/ft³ (kg/m³)
- σ sidewash angle, deg
- φ angle of bank, deg or rad
- ψ angle of yaw, deg or rad

$$C_{l\beta} = \frac{\partial C_l}{\partial \beta} \qquad C_{n\beta} = \frac{\partial C_n}{\partial \beta} \qquad C_{Y\beta} = \frac{\partial C_Y}{\partial \beta}$$

$$C_{lp} = \frac{\partial C_l}{\partial \frac{pb}{2V}} \qquad C_{np} = \frac{\partial C_n}{\partial \frac{pb}{2V}} \qquad C_{Yp} = \frac{\partial C_Y}{\partial \frac{pb}{2V}}$$

$$C_{lr} = \frac{\partial C_l}{\partial \frac{rb}{2V}} \qquad C_{nr} = \frac{\partial C_n}{\partial \frac{rb}{2V}} \qquad C_{Yr} = \frac{\partial C_Y}{\partial \frac{rb}{2V}}$$

$$C_{n\beta, \text{dynamic}} = C_{n\beta} - \frac{I_Z}{I_X} C_{l\beta} \sin \alpha$$

$\Delta C_{n\beta_v}$ increment of $C_{n\beta}$ due to vertical tail

Model component designations:

F fuselage

H horizontal tail

V vertical tail

W wing

DESCRIPTION OF AIRPLANE

The airplane studied in the investigation is a two-place twin-jet high-performance fighter designed for land and carrier-based operations. A three-view sketch showing the general layout of the configuration is presented in figure 1, geometric characteristics of the airplane are listed in table I, and typical mass characteristics for normal flight operations (no external stores) are presented in table II. The longitudinal control system of the airplane consists of an all-movable horizontal tail (stabilator) which incorporates 23° negative dihedral (droop) to satisfy longitudinal stability requirements in the normal operational flight range. The airplane lateral control system consists of upper-surface spoilers and ailerons. The control system is mechanized such that the ailerons deflect downward only while the spoilers deflect upward. The left aileron and right spoiler operate simultaneously as do the right aileron and left spoiler. The directional control system consists of a conventional rudder. The maximum control-surface deflections are as follows:

Rudder deflection, deg	±30
Stabilator deflection (trailing edge), deg.	21 up, 9 down
Aileron deflection, deg	0 up, 30 down
Spoiler deflection, deg	45 up, 0 down

Mass loadings such as those presented in table II are typical of those of modern high-performance fighter airplanes and result from the fact that the major portion of the airplane mass is distributed along the fuselage; therefore the values of I_Z and I_Y are several times as great as those of I_X . This type of inertial distribution has significant

effects on dynamic lateral-directional stability at high angles of attack as is discussed subsequently.

FLIGHT MOTIONS

The directional divergence exhibited by the airplane at high angles of attack is illustrated by the time histories presented in figure 2. Shown in figure 2 are flight recorder traces of the major flight variables and control-surface deflections during an accelerated stall at 25 000 feet (7620 m) with the airplane configured for cruise flight ($M = 0.4$). Unfortunately there is no record of yaw angle or yaw rate. The maneuver was initiated by rolling to a 60° banked turn to the left. Angle of attack was then increased at an approximately constant rate. The normal acceleration trace indicates airframe buffet occurred at angles of attack as low as 10° . At about 38 seconds the magnitude of the normal acceleration trace starts to decrease, even though angle of attack is increasing, thereby indicating major stall. The angle of attack at this time was about 18° ; this value should be remembered when analyzing the force test results presented subsequently. As the angle of attack increased further, lightly damped lateral oscillations about the longitudinal body axis (termed "wing rock") became noticeable. At about 44 seconds severe wing rock was experienced; at about 50 seconds the oscillation diverged violently and the airplane entered a $2\frac{1}{2}$ -turn spin to the right. The flight path was about 40° below the horizon during the spin; therefore the spin appears as a continuous roll with reference to the earth axes. The angle of attack at the time of directional divergence was between 20° and 25° ; this range of angle of attack should also be remembered for subsequent reference.

METHOD OF ANALYSIS

Static wind-tunnel force tests were conducted to determine the aerodynamic characteristics of the airplane at high angles of attack. Airframe components were tested individually and in several combinations to determine the contributions of the isolated components to the overall stability characteristics of the airplane and to determine mutual interference effects. Several geometric modifications or fixes to the basic configuration were evaluated in an attempt to delay or eliminate lateral-directional instability near the stall.

The dynamic stability characteristics of the airplane were calculated by using linear three-degree-of-freedom equations of motion. The static and dynamic aerodynamic stability derivatives used as input data in these calculations were measured quantities determined in wind-tunnel tests of a model of the airplane.

Model and Test Equipment

The wind-tunnel data presented herein were obtained with a 1/11-scale model tested at the Langley Research Center in a low-speed wind tunnel with a 12-foot (3.66-m) octagonal test section. Additional data obtained at higher values of Reynolds number during tests of a 1/15-scale model at the Ames Research Center are also presented for purposes of correlation. The two models differed in external engine inlet configuration and horizontal tail leading-edge configuration as shown in figure 3 – the inlets and horizontal tail of the 1/11-scale model being representative of those of an earlier airplane configuration and the inlets and horizontal tail of the 1/15-scale model being representative of those of a later airplane configuration. Both models had blocked inlets – that is, flow through the engines was not simulated. A number of geometric modifications to the basic airplane configuration were evaluated as possible fixes for the lateral-directional stability problem during the course of the study. These modifications, summarized in figure 4, consisted of vertical end plates on the stabilator, afterbody strakes, nose strakes, wing apex notches, wing fences, wing leading-edge droop, and two modified vertical tail surfaces.

Tests

Wind-tunnel force tests of the 1/11-scale model were conducted at low-subsonic speeds at a Reynolds number of 0.5×10^6 based on the mean aerodynamic chord of the wing. Measurements were made of the six force and moment components over an angle-of-attack range from 0° to 40° for a range of angle of sideslip of $\pm 40^\circ$. The wing, fuselage, vertical tail, and horizontal tail were tested in several combinations. Tuft-flow visualization tests were conducted to aid in the interpretation and understanding of the force test results. A limited number of dynamic-pressure and sidewash measurements at the vertical tail location were also made in conjunction with an analysis of the effectiveness of the vertical tail at high angles of attack. Additional low-subsonic force test data measured at a Reynolds number of 4.3×10^6 at the Ames Research Center are also presented.

Calculations

The dynamic stability characteristics of the lateral-directional modes of motion were calculated for the basic and modified airplane configurations by using the linearized three-degree-of-freedom equations of motion presented in appendix A. The calculated characteristics included the period P and time to half-amplitude $t_{1/2}$ of the Dutch roll mode and the time to half-amplitude of the spiral and roll subsidence modes. The magnitude and phase relationships of the roll ϕ , yaw ψ , and sideslip β angles were also calculated to indicate the "shape" or general nature of the Dutch roll mode. Values of the dynamic lateral-directional stability derivatives used in the calculations were obtained from the results of unpublished forced-oscillation tests of the 1/11-scale model.

Dynamic stability calculations were made for trimmed level flight at an altitude of 25 000 feet (7620 m). Mass characteristics used in the calculations are given in table II and the aerodynamic stability derivatives used are summarized in table III.

RESULTS OF FORCE TESTS

The present paper presents a general discussion of the results of all the pertinent force tests run during the study; however it presents only samples of the detailed data as needed to support the analysis. The results of the force tests are analyzed in terms of the individual contributions of the various airframe components to the overall aerodynamic stability parameters.

Longitudinal Stability Characteristics

Basic configuration.- The static longitudinal characteristics of the basic configuration obtained during the force test program are presented in figure 5. The data denoted by a circular symbol are those obtained at low values of Reynolds number at the Langley Research Center; whereas the square symbols denote data obtained at considerably higher values of Reynolds number at the Ames Research Center. The data indicate good agreement between the high and low Reynolds number lift characteristics with the exception of the immediate poststall angle-of-attack range of 20° and 40° . These differences are believed to be due to the combined effects of Reynolds number and the geometric model differences mentioned previously. The variation of lift coefficient with angle of attack indicates that the lift-curve slope begins to decrease at an angle of attack of about 15° . Associated with the apparent flow separation is a reduction in the level of longitudinal stability. The low Reynolds number data indicate a condition of neutral longitudinal stability from $\alpha = 15^\circ$ to $\alpha = 20^\circ$; whereas the high Reynolds number data indicate a mild instability or pitch-up tendency for the same angle-of-attack range. This pitch-up tendency has been verified during stall entries with the full-scale airplane. The significance of the longitudinal aerodynamic characteristics in relation to the lateral-directional stability of the airplane at the stall is twofold. First, the progression of major wing stall at an angle of attack of 15° should be reflected in changes in the lateral-directional aerodynamic characteristics at the same angle of attack; and second, the existence of longitudinal instability at the stall would be expected to aggravate an already deteriorating control problem and cause the pilot to overshoot to the higher angles of attack associated with directional divergence.

Modified configuration.- The effect of drooping the wing leading edge (40°) on longitudinal characteristics is shown in figure 6. It can be seen that the drooped leading edge maintained the linear portion of the lift curve up to $\alpha = 20^\circ$ and increased the value of the maximum lift coefficient. The leading-edge droop also reduced the longitudinal

stability to such an extent that the configuration became neutrally stable over a much wider range of angle of attack. This reduction in stability is believed to be the result of leading-edge separation which is highly sensitive to variations in Reynolds number.

Lateral-Directional Characteristics

Basic configuration.- The variation of the static lateral-directional force and moment coefficients with angle of sideslip for the basic configuration are presented in figure 7. As can be seen, the variations of the lateral-directional coefficients were generally linear over a sideslip range of $\pm 20^\circ$. Stability derivatives obtained over a range of sideslip angle of $\pm 5^\circ$ are summarized in figure 8. The values of the stability derivatives are presented as the variations with angle of attack of the side-force derivative $C_{Y\beta}$, the directional-stability derivative $C_{n\beta}$, and the effective-dihedral derivative $C_{l\beta}$. The circular symbols represent data obtained at a Reynolds number of 0.5×10^6 ; whereas the square symbols denote data obtained at a Reynolds number of 4.3×10^6 . The two sets of data agree fairly well with the exception of a slightly lower level of directional stability for the higher Reynolds number data at moderate angles of attack. Both sets of data indicate a marked decrease in $C_{n\beta}$ as angle of attack is increased with the directional stability being negative at angles of attack above 22° . The data also indicate that as the angle of attack exceeds 15° a substantial reduction in effective dihedral occurs, as might be expected from the lift curves presented in figure 5. Actually the loss of directional stability at $\alpha = 22^\circ$ is considered to be especially serious because of the corresponding loss of effective dihedral. This aspect of the problem is discussed in detail subsequently. Also shown in figure 8 is a vertical hatched region indicating the maximum trim capability of the horizontal tail based on static force tests ($i_t = -21^\circ$). It can be seen that there exists a trimmed angle-of-attack range of almost 10° for which the airplane is directionally unstable.

Effect of airframe components.- The results of a series of tests to evaluate the contributions of various airframe components to the directional-stability derivative $C_{n\beta}$ are summarized in figure 9. Data obtained for the isolated wing and fuselage are presented in figure 9(a) along with data obtained for the wing-fuselage combination. The data of figure 9(b) show the effects of the addition of the horizontal and vertical tail surfaces to the wing-fuselage combination; and the data of figure 9(c) show the effects of the addition of the vertical tail to the isolated fuselage. Several points are to be noted from comparisons of the various data. For example, the isolated wing data W of figure 9(a) indicate little variation of $C_{n\beta}$ (relative to body axes) with increase in angle of attack. This result is to be expected inasmuch as little if any leading-edge suction is developed on thin sweptback wings. Also the isolated fuselage data F show that the fuselage does

not become more unstable until the angle of attack exceeds 28° . The wing-fuselage combination WF, however, shows large unstable variations of $C_{n\beta}$ with increasing angle of attack. The magnitudes of $C_{n\beta}$ are far greater than those expected by simple addition of the values for the isolated wing and fuselage. This type of aerodynamic phenomenon has been noted in the past for sweptback wing-fuselage combinations at high angle of attack (ref. 1). As stated in reference 1, the large unstable variations of directional stability which exist relative to the body axes are due largely to wing (or wing-fuselage) induced sidewash over the fuselage afterbody. An additional factor to be considered is the fact that when a swept-wing configuration is sideslipped at high angles of attack, leading-wing-panel stall may significantly affect the flow pattern at the rear of the airplane. This fact is illustrated subsequently by tuft photographs.

The adverse sidewash characteristics exhibited by the wing-fuselage combination might be expected to affect adversely the contributions of the vertical and horizontal tails to directional stability. The data of figure 9(b) support this assumption by showing that (1) the addition of the drooped horizontal tail H to the wing-fuselage combination WF produced a large destabilizing effect at high angles of attack, and (2) the vertical tail contribution to directional stability diminishes markedly as α is increased above 20° and becomes destabilizing at angles of attack above 30° .

The fact that the wing-fuselage combination, and not the fuselage itself, was responsible for the loss in tail effectiveness at high angles of attack is indicated by the data of figure 9(c) which show a comparison of the directional stability characteristics of the fuselage and vertical tail combination and the fuselage alone. This comparison shows that the vertical tail contribution at high angles of attack was reduced only slightly in comparison to the large loss in tail effectiveness shown by figure 9(b) when the tail was added to the wing-fuselage combination. The data of figure 9(c) show however that the effectiveness of the vertical tail at high angles of attack for the fuselage-tail combination was only about one-half as great as at low angles of attack. It is possible that this loss in tail effectiveness (note that the tail was never destabilizing) could have been partly or entirely the result of a reduction of dynamic pressure at the tail because of shielding by the fuselage at high angles of attack.

In order to evaluate the adverse sidewash and reduction in dynamic pressure at the vertical tail location, measurements were made of the dynamic pressure and sidewash angle at the tail location. The results of the tests are shown as functions of angle of attack in figure 10.

The results of the pressure survey are presented as q_v/q_∞ , the ratio of dynamic pressure at the vertical tail location divided by the free-stream dynamic pressure. The dynamic-pressure ratio is reduced as angle of attack is increased above 15° . More specifically, as the stall angle of attack is exceeded, the ratio is reduced to less than

50 percent of the value at $\alpha = 0^\circ$ because of combined shielding of the vertical tail by the fuselage afterbody and impingement of the low velocity wake of the stalled wing-fuselage combination on the vertical tail.

The sidewash angles at the vertical tail location were determined by comparing vertical tail-off data with data obtained by deflecting the vertical tail as an all-movable tail at various angles of sideslip relative to the fuselage. The results of the sidewash measurements are presented in terms of the sidewash parameter $1 - \frac{\partial \sigma}{\partial \beta}$. At low angles of attack, the data of figure 10 indicate that the sidewash is quite favorable, as has been noted in the past for low-wing configurations. (See refs. 2 to 4.) At angles of attack near the stall, however, the sidewash parameter changes from favorable to unfavorable and, at $\alpha = 30^\circ$, the factor becomes negative, thereby indicating the existence of a destabilizing flow field at the vertical tail location.

The foregoing data and analysis show that the primary factor producing loss of directional stability at angles of attack immediately below the stall (angles in the 15° to 20° range) is adverse sidewash on the fuselage afterbody and drooped horizontal tail induced by the wing-fuselage combination. As α is increased above a value of about 20° , the vertical tail enters the adverse sidewash field and the dynamic pressure at the vertical tail is reduced because of shielding by the aft fuselage and/or the stalled wake of the wing. Both of these factors contribute to a loss of vertical tail effectiveness at high angles of attack. The adverse sidewash effect is the predominant effect at angles of attack above 30° where the tail contribution to directional stability actually becomes negative.

Modified configuration.- A number of geometric configuration modifications were tested in an effort to delay the loss of directional stability to higher angles of attack. Test results obtained with the modifications shown in figure 4(a) had no appreciable effect on either the angle of attack at which directional stability was lost or on the loss of effective dihedral above $\alpha = 15^\circ$. These results are therefore not presented in this paper.

A second series of modifications was aimed at evaluation of the vertical tail size necessary to delay or eliminate the loss of directional stability. The results of tests conducted with the modified vertical tail surfaces shown in figure 4(c) are presented in figure 11. Increasing the aspect ratio or area of the basic vertical tail by 100 percent increased the directional stability at low angles of attack; however the configuration remained directionally unstable for angles of attack greater than 25° . It is interesting to note that increasing the vertical tail area made the configuration more unstable above $\alpha = 30^\circ$ as would be expected based on the results of the sidewash measurements discussed in the previous section. Increasing the aspect ratio did not produce this trend

probably because the increase in aspect ratio added vertical tail area above the adverse sidewash field.

Inasmuch as it was determined that the wing-fuselage combination was a major factor leading to directional instability, tests were conducted to modify the basic-wing aerodynamic characteristics. It has been noted that the subject airplane appears to be more prone to exhibit directional divergence in the cruise configuration than in the landing-approach configuration (leading-edge slats, flaps, and gear extended). The airplane in the landing-approach configuration can consistently be flown at the same angles of attack at which the cruise configuration exhibits violent lateral-directional instability. This difference is believed to be attributable to the effect of the extended slats and flaps on the aerodynamic characteristics of the wing-fuselage combination. Inasmuch as the full-scale airplane wing slats are equipped with boundary-layer control which is difficult to simulate at small scale, it was decided to obtain a gross indication of the effects of these devices by drooping the leading edge of the wing as shown in figure 4(b). The results of tests showing the effect of 40° leading-edge droop angle on $C_{n\beta}$ and $C_{l\beta}$ are presented in figure 12. The data indicate that leading-edge droop produced two very significant and beneficial effects. First, the angle of attack at which directional stability was lost was increased from 22° to 25° ; and second, $C_{l\beta}$ was maintained at moderate levels up to $\alpha = 40^\circ$. These changes, especially the increase in $C_{l\beta}$ at high angles of attack, have important beneficial effects on dynamic lateral-directional stability, as is shown subsequently herein. Additional tests were conducted to determine whether the increase in $C_{n\beta}$ at $\alpha = 25^\circ$ was due to wing-fuselage characteristics or vertical tail effectiveness; the results of the tests are shown in figure 13. The increase in $C_{n\beta}$ appears to be related to both of these factors and is primarily an extension of vertical tail effectiveness to $\alpha = 25^\circ$.

The previous results were obtained with both inner and outer panels of the wing leading edge deflected. (See fig. 4(b).) Several combinations involving various droop angles and leading-edge panels were tested; however the most effective combination was found to be 40° leading-edge droop on both inner and outer panels.

RESULTS OF TUFT STUDIES

A series of tuft studies were conducted to aid in the interpretation of the static force test results. Photographs of the tuft patterns as α is increased for sideslip angles of 0° and -10° are presented in figure 14. At $\alpha = 0^\circ$, sideslip induces a strong favorable sidewash field at the vertical tail, as can be seen by the relative angles of the tufts on the fuselage afterbody. This result is in agreement with the results previously presented regarding variations of $1 - \frac{\partial \sigma}{\partial \beta}$. As the angle of attack is increased, however, the favorable sidewash angle is reduced. At $\alpha = 25^\circ$ and $\beta = -10^\circ$, the tuft patterns indicate a

complete stall of the leading-wing panel and a reversed-flow region behind the stalled wing panel. This reversed-flow region is evident from the tufts on the fuselage behind the wing, and an extensive region of reversed or low-velocity flow in the vicinity of the vertical tail was found by exploring with a tuft on a wand. This reversed-flow and low-velocity region behind the stalled wing and fuselage is evidently the cause of the reduction of q_v/q_∞ at the rear of the model, shown in figure 10, and is a major factor contributing to the directional instability of the wing-fuselage combination and to the loss in vertical tail effectiveness at high angles of attack. The results of the tuft studies also indicate that stall of the leading-edge panel is the cause of the loss of effective dihedral at $\alpha = 15^\circ$. Such a result is a characteristic of swept wings at high angles of attack.

RESULTS OF DYNAMIC STABILITY CALCULATIONS

The results of calculations to determine the lateral-directional dynamic stability of the basic configuration and of the modified configuration (incorporation of wing leading-edge droop) are presented in figure 15 and table III. These results should be interpreted as qualitative (rather than quantitative) indications of the dynamic stability of the airplane for several reasons. First, the application of small perturbation, linearized equations of motion near the stall may be questionable because of the large amplitude motions involved (see fig. 2) and also because of the extremely nonlinear variations of yawing moment with angle of sideslip exhibited by the configuration at high angles of attack. (See fig. 7.) A second area of concern is that large variations in values of dynamic derivatives with amplitude and frequency at angles of attack near the stall have been noted in past investigations. Also the calculations made for the modified configuration assumed changes in only the static stability derivatives $C_{n\beta}$, $C_{l\beta}$, and $C_{Y\beta}$ and neglected possible variations in dynamic derivatives because of wing leading-edge droop. The calculated results should however serve as a gross indication of the dynamic behavior of the vehicle for small disturbances from trimmed flight at large angles of attack.

Basic Configuration

The variation with angle of attack of the damping characteristics of the various modes of motion for the basic configuration are presented in the upper plot of figure 15(a). The damping of the roll, spiral, and Dutch roll modes are presented in terms of the damping factor $\frac{1}{t_{1/2}}$. Positive values of $\frac{1}{t_{1/2}}$ represent damped (dynamically stable) modes while negative values represent undamped (dynamically unstable) modes. The results of the calculations indicate that as α is increased, the roll and spiral modes of motion remain stable with the exception of the spiral mode at angles of attack between 18° and 22° . The unstable spiral mode indicated by the calculations has not however been evident in flight test results. The calculated results also indicate that the Dutch roll

oscillation becomes lightly damped at the stall and becomes unstable at an angle of attack of about 23° . This result agrees with the flight data presented in figure 2. The relative magnitudes and phase relationships of the roll-to-sideslip ratio ϕ/β and roll-to-yaw ratio ϕ/ψ presented in table III indicate the general nature of the lateral oscillation. The data indicate that as α is increased up to 15° , the magnitude of ϕ/ψ is increased and the phase relationship of ϕ/β approaches zero, thereby indicating that the Dutch roll becomes predominately a rolling motion about the longitudinal axis. This result is also in agreement with flight experience. At the poststall angles of attack ($\alpha = 25^\circ$ and 30°), the phase and magnitude relationships change such that the magnitude of ϕ/ψ is considerably reduced and ϕ and ψ become approximately in phase. These characteristics are indicative of larger yawing content in the Dutch roll mode which would, because of the relative phasing of ϕ and ψ and the high degree of instability (time required to double amplitude less than 2 seconds), appear to the pilot as a yawing or directional divergence. These results indicate that the directional divergence exhibited by the airplane is in reality a highly unstable Dutch roll oscillation, the character of which changes from that of a predominately rolling motion at prestall angles of attack to that of a predominately yawing motion at poststall angles of attack.

In the past, numerous investigations of lateral-directional dynamic stability at high angles of attack have been conducted. (For example, see refs. 5 to 9.) One common and significant outcome of the studies was the indication that configurations having relatively high values of the ratio I_Z/I_X together with appreciable values of the effective-dihedral parameter $-C_{l\beta}$ usually diverge under dynamic flight conditions at angles of attack higher than those expected based on the variation of $C_{n\beta}$ with α . This characteristic is attributed to the favorable effect of $-C_{l\beta}$ on dynamic stability as described in appendix B. As a result of past experience the parameter $C_{n\beta, \text{dynamic}}$ is usually used as an indication of directional divergence at high angles of attack. Shown in the lower plot of figure 15(a) are the variations of $C_{n\beta}$ and $C_{n\beta, \text{dynamic}}$ with angle of attack for the basic configuration. The data show that $C_{n\beta}$ and $C_{n\beta, \text{dynamic}}$ approach zero at a common angle of attack of about 21° . This result is attributable to the reduction of $-C_{l\beta}$ at the stall as noted in figure 8. The angle of attack at which $C_{n\beta, \text{dynamic}}$ becomes negative does give a good approximation of the angle of attack at which the damping of the Dutch roll mode becomes unstable.

Modified Configuration

The results of the calculations for the airplane with 40° leading-edge droop are presented only to illustrate the effects of leading-edge devices on lateral-directional stability. Leading-edge droop is not proposed herein as an acceptable modification to the airplane because of the reduction of longitudinal stability shown in figure 6.

The variation of the damping of the lateral-directional modes of motion for the modified configuration are shown in the upper plot of figure 15(b). The data indicate that all modes of motion remain dynamically stable up to $\alpha = 30^\circ$. The elimination of dynamic instability is produced by the increases in $C_{n\beta}$ and $C_{l\beta}$ given in figure 12. The lower plot in figure 15(b) indicates that $C_{n\beta, \text{dynamic}}$ also remained positive up to $\alpha = 30^\circ$ because of the moderate level of $C_{l\beta}$ afforded by leading-edge droop.

The results obtained with leading-edge droop indicate that leading-edge devices can significantly alter the dynamic lateral-directional behavior of the present configuration. The effects of leading-edge droop are believed to be similar to those obtained with the airplane configured for the power approach. The foregoing analysis explains why the airplane remains dynamically stable in the approach configuration. It should also be emphasized that the gains afforded by high-lift devices are limited and that the airplane would become unstable at higher angles of attack.

CONCLUSIONS

The results of an analysis of the lateral-directional stability characteristics of a twin-jet swept-wing fighter airplane at high angles of attack indicate the following conclusions:

1. The directional divergence exhibited by the airplane is brought about by a simultaneous loss of directional stability and effective dihedral at high angles of attack.
2. The loss of directional stability results from a combination of an adverse sidewash region at the rear of the airplane and a reduced dynamic pressure at the vertical tail location. The adverse sidewash is generated by the wing-fuselage combination and is related to stalling of the leading wing during sideslip at high angles of attack.
3. The loss of effective dihedral is a result of stalling of the leading-wing panel at high angles of attack.
4. The apparent directional divergence is in reality part of one cycle of a highly unstable Dutch roll oscillation.
5. The only geometric modification studied that significantly delayed the divergence was wing leading-edge droop. The leading-edge droop however reduced the level of longitudinal stability for the low value of Reynolds number used in the tests.

Langley Research Center,
National Aeronautics and Space Administration,
Langley Station, Hampton, Va., June 4, 1969,
126-62-01-01-23.

APPENDIX A

EQUATIONS OF MOTION

The nondimensional lateral-directional equations of motion referred to a principal body-axis system are as follows:

Roll:

$$-2\mu_b K_{X_0}^2 D_b^2 \phi + C_{l\beta} \beta + \frac{1}{2} C_{lp} D_b \phi + \frac{1}{2} C_{lr} D_b \psi = 0$$

Yaw:

$$-2\mu_b K_{Z_0}^2 D_b^2 \psi + C_{n\beta} \beta + \frac{1}{2} C_{np} D_b \phi + \frac{1}{2} C_{nr} D_b \psi = 0$$

Sideslip:

$$\begin{aligned} & -2\mu_b (D_b \beta + \cos \alpha D_b \psi) + C_{Y\beta} \beta + \frac{1}{2} C_{Yp} D_b \phi + 2\mu_b \sin \alpha D_b \phi \\ & + C_L \sin \alpha \psi + C_L \cos \alpha \phi + \frac{1}{2} C_{Yr} D_b \psi = 0 \end{aligned}$$

When $\phi_0 e^{\lambda s_b}$ is substituted for ϕ , $\psi_0 e^{\lambda s_b}$ for ψ , and $\beta_0 e^{\lambda s_b}$ for β in the equations written in determinant form, λ must be a root of the characteristic equation (neglecting the zero or heading root)

$$A\lambda^4 + B\lambda^3 + C\lambda^2 + D\lambda + E = 0$$

where

$$A = 8\mu_b^3 K_{X_0}^2 K_{Z_0}^2$$

$$B = -2\mu_b^2 (2K_{X_0}^2 K_{Z_0}^2 C_{Y\beta} + K_{X_0}^2 C_{nr} + K_{Z_0}^2 C_{lp})$$

$$\begin{aligned} C = \mu_b \left(-K_{X_0}^2 C_{Yr} C_{n\beta} + K_{X_0}^2 C_{nr} C_{Y\beta} + 4\mu_b K_{X_0}^2 C_{n\beta} \cos \alpha + K_{Z_0}^2 C_{lp} C_{Y\beta} \right. \\ \left. - K_{Z_0}^2 C_{l\beta} C_{Yp} - 4\mu_b K_{Z_0}^2 C_{l\beta} \sin \alpha + \frac{1}{2} C_{nr} C_{lp} - \frac{1}{2} C_{np} C_{lr} \right) \end{aligned}$$

APPENDIX A

$$\begin{aligned}
 D = & -\mu_b \left(2K_{X_0}^2 C_{n\beta} C_L \sin \alpha + 2K_{Z_0}^2 C_{l\beta} C_L \cos \alpha + C_{n\beta} C_{l_r} \sin \alpha - C_{l\beta} C_{n_r} \sin \alpha \right. \\
 & \left. + C_{n\beta} C_{l_p} \cos \alpha - C_{l\beta} C_{n_p} \cos \alpha \right) - \frac{1}{4} \left(C_{n_r} C_{l_p} C_{Y\beta} + C_{n_r} C_{l\beta} C_{Y_p} - C_{n_p} C_{Y_r} C_{l\beta} \right. \\
 & \left. + C_{n_p} C_{l_r} C_{Y\beta} - C_{n\beta} C_{Y_p} C_{l_r} + C_{n\beta} C_{Y_r} C_{l_p} \right)
 \end{aligned}$$

$$E = \frac{1}{2} C_L \cos \alpha \left(C_{n_r} C_{l\beta} - C_{l_r} C_{n\beta} \right) + \frac{1}{2} C_L \sin \alpha \left(C_{l_p} C_{n\beta} - C_{n_p} C_{l\beta} \right)$$

The period and damping of a mode of motion in seconds are given, respectively, by the equations

$$P = \frac{2\pi}{d} \frac{b}{V}$$

and

$$t_{1/2} = - \frac{0.693}{c} \frac{b}{V}$$

where c and d are the real and imaginary parts of the root of the characteristic equation.

APPENDIX B

INTERPRETATION OF $C_{n\beta, \text{dynamic}}$

During the course of the study, it was observed that the lateral-directional divergence occurring in the poststall region was not an aperiodic divergence but rather a violently unstable oscillation. Inasmuch as the parameter

$$C_{n\beta, \text{dynamic}} = C_{n\beta} - \frac{I_Z}{I_X} C_{l\beta} \sin \alpha$$

has been shown to correlate with directional divergence of inertially slender configurations, an attempt was made to correlate the calculated oscillatory instability with the parameter $C_{n\beta, \text{dynamic}}$. It was observed that the oscillatory instability was associated with a change in sign of the coefficient C of the characteristic equation. (See appendix A.) This particular coefficient contains several combinations of derivatives; however most of the magnitude of the coefficient is composed of the term

$$4\mu_b \left(K_{X_0}^2 C_{n\beta} \cos \alpha - K_{Z_0}^2 C_{l\beta} \sin \alpha \right)$$

This expression $C_{n\beta, \text{dynamic}} > 0$ therefore is an approximate criterion for divergence in the form of lateral-directional oscillatory instability.

REFERENCES

1. Polhamus, Edward C.; and Spreemann, Kenneth P.: Subsonic Wind-Tunnel Investigation of the Effect of Fuselage Afterbody on Directional Stability of Wing-Fuselage Combinations at High Angles of Attack. NACA TN 3896, 1956.
2. Goodman, Alex: Effects of Wing Position and Horizontal-Tail Position on the Static Stability Characteristics of Models With Unswept and 45° Sweptback Surfaces With Some Reference to Mutual Interference. NACA TN 2504, 1951.
3. Goodman, Alex; and Thomas, David F., Jr.: Effects of Wing Position and Fuselage Size on the Low-Speed Static and Rolling Stability Characteristics of a Delta-Wing Model. NACA Rep. 1224, 1955. (Supersedes NACA TN 3063.)
4. Queijo, M. J.; and Wolhart, Walter D.: Experimental Investigation of the Effect of Vertical-Tail Size and Length and of Fuselage Shape and Length on the Static Lateral Stability Characteristics of a Model With 45° Sweptback Wing and Tail Surfaces. NACA Rep. 1049, 1951. (Supersedes NACA TN 2168.)
5. Moul, Martin T.; and Paulson, John W.: Dynamic Lateral Behavior of High-Performance Aircraft. NACA RM L58E16, 1958.
6. Shanks, Robert E.: Investigation of the Low-Subsonic Flight Characteristics of a Model of an All-Wing Hypersonic Boost-Glide Configuration Having Very High Sweep. NASA TN D-369, 1960.
7. Boisseau, Peter C.: Investigation of the Low-Subsonic Flight Characteristics of a Model of a Reentry Vehicle With a Thick Flat 75° Swept Delta Wing and a Half-Cone Fuselage. NASA TN D-1007, 1962.
8. Freeman, Delma C., Jr.: Low-Subsonic Flight and Force Investigation of a Supersonic Transport Model With a Double-Delta Wing. NASA TN D-4179, 1968.
9. Freeman, Delma C., Jr.: Low Subsonic Flight and Force Investigation of a Supersonic Transport Model With a Variable-Sweep Wing. NASA TN D-4726, 1968.

TABLE I.- DIMENSIONAL CHARACTERISTICS OF AIRPLANE

Overall length	57.59 ft (17.55 m)
Wing:	
Span	38.41 ft (11.71 m)
Area (including leading-edge extension)	538.34 ft ² (50.01 m ²)
Root chord	282.00 in. (716.28 cm)
Tip chord	47.00 in. (119.38 cm)
Mean aerodynamic chord, \bar{c}	192.50 in. (488.95 cm)
Leading edge of \bar{c} rearward of leading edge of root chord	110.76 in. (281.33 cm)
Aspect ratio	2.82
Taper ratio	0.167
Sweepback of 25 percent chord	45.00°
Dihedral (inboard 69.5 percent $b/2$)	0°
Dihedral (outboard 69.5 percent $b/2$)	12.00°
Incidence	1.00°
Airfoil section:	
Root	NACA 0006.4-64 (modified)
Tip	NACA 0003.0-64 (modified)
Aileron:	
Area (one side) rearward of hinge line	13.08 ft ² (1.22 m ²)
Span (one aileron) (from 44.5 percent $b/2$ to 67.0 percent $b/2$)	4.35 ft (1.33 m) (22.5 percent $b/2$)
Inboard end chord (base line 103.24 in. (262.23 cm))	37.81 in. (96.04 cm) (21.3 percent \bar{c})
Outboard end chord (base line 155.44 in. (394.82 cm))	34.38 in. (87.33 cm) (27.6 percent \bar{c})
Spoilers:	
Area (one side)	13.08 ft ² (1.22 m ²)
Span (from 45.3 percent $b/2$ to 67.0 percent $b/2$)	4.19 ft (1.28 m)
Inboard end chord	1.39 ft (0.42 m)
Outboard end chord	1.04 ft (0.32 m)
Horizontal tail:	
Area (in chord plane)	94.70 ft ² (8.80 m ²)
Movable area	77.40 ft ² (7.19 m ²)
Span	17.705 ft (5.40 m)
Aspect ratio	3.30
Taper ratio	0.20
Sweepback of 25-percent chord	35.50°

TABLE I.- DIMENSIONAL CHARACTERISTICS OF AIRPLANE - Concluded

Dihedral	-23.00°
Root chord (at airplane center line)	107.00 in. (271.78 cm)
Tip chord (theoretical)	21.40 in. (54.36 cm)
Airfoil section:	
Root (airplane center line)	NACA 0003.7-64 (modified)
Tip (theoretical)	NACA 0003.0-64 (modified)
Hinge-line location, percent \bar{c}_t	41.00
Vertical tail:	
Area	67.50 ft ² (6.27 m ²)
Span	6.38 ft (1.94 m)
Taper ratio	0.227
Root chord	207.15 in. (526.16 cm)
Tip chord	47.10 in. (119.63 cm)
Sweepback of 25-percent chord	58.30°
Airfoil section:	
Root	NACA 0004.0-64 (modified)
Tip	NACA 0002.5-64 (modified)
Rudder:	
Area (rearward of hinge line)	11.07 ft ² (1.03 m ²)
Hinge-line location, percent of water-line chords	80.00

TABLE II.- MASS AND INERTIA CHARACTERISTICS OF AIRPLANE

Weight, lb (N)	39 099 (173 912)
Center-of-gravity position (percent \bar{c})	33
Relative density, μ_b :	
Sea level	24.73
25 000 ft (7620 m)	55.16
Moments of inertia:	
I_X , slug-ft ² (kg-m ²)	29 950 (35 183)
I_Z , slug-ft ² (kg-m ²)	169 538 (229 860)
I_{XZ} , slug-ft ² (kg-m ²)	5241 (7106)

TABLE III.- CALCULATED DYNAMIC STABILITY CHARACTERISTICS

α , deg	$C_{Y\beta}'$ per rad	$C_{n\beta}'$ per rad	$C_{l\beta}'$ per rad	C_{Yp}' per rad	C_{np}' per rad	C_{lp}' per rad	C_{Yr}' per rad	C_{nr}' per rad	C_{lr}' per rad	Spiral mode	Dutch roll mode						
											$t_{1/2}$, sec	Roll mode	$t_{1/2}$, sec	P, sec		Phase, deg	
														$t_{1/2}$, sec	ϕ/β		ϕ/ψ
Basic configuration																	
10	-0.6251	0.1037	-0.1226	0.0000	-0.0100	-0.3030	1.1210	-0.6370	0.1870	10.23	0.707	2.37	3.60	3.34	7.58	21	-142
15	-.5730	.0808	-.1570	.2460	.0000	-.2170	1.1060	-.6060	.3050	6.62	1.329	3.32	3.53	3.14	17.15	11	-150
20	-.4355	.0212	-.0023	.1180	.0100	-.3140	.8800	-.6160	.6160	a-4.28	.954	2.14	15.92	2.76	2.62	99	-33
25	-.2716	-.1587	.0115	.0300	.0420	-.4210	.3050	-.8780	.8830	1.34	.333	a-1.50	17.77	5.18	1.64	109	-9
30	-.1604	-.2126	-.0115	.0560	-.0310	-.4100	-.7080	-.4440	.6380	1.27	.353	a-1.41	14.78	7.78	1.63	104	-6
Modified configuration																	
10	-0.6039	0.1203	-0.1524	0.0000	-0.0100	-0.3030	1.1210	-0.6370	0.1870	9.23	0.740	2.61	3.45	3.49	8.52	19	-144
15	-.5283	.0768	-.1467	.2460	.0000	-.2170	1.1060	-.6060	.3050	6.74	1.328	3.22	3.58	3.13	16.61	11	-150
20	-.5661	.0756	-.1215	.1180	.0100	-.3140	.8800	-.6160	.6160	19.97	1.49	2.13	4.15	2.42	12.10	14	-137
25	-.4149	.0115	-.0562	.0300	.0420	-.4210	.3050	-.8780	.8830	4.30	1.66	1.42	6.81	2.50	38.1	12	-61
30	-.3392	-.1513	-.0619	.0560	-.0310	-.4100	-.7080	-.4440	.6380	(b)	(b)	a-12.39	9.32	7.99	2.43	35	3

^aNegative values of $t_{1/2}$ indicate unstable modes of motion. For example, $t_{1/2} = -2$ indicates time required to double amplitude of 2 sec.

^bSpiral and roll modes combine to form second lateral oscillation having $t_{1/2} = 0.91$ sec and $P = 18.7$ sec.

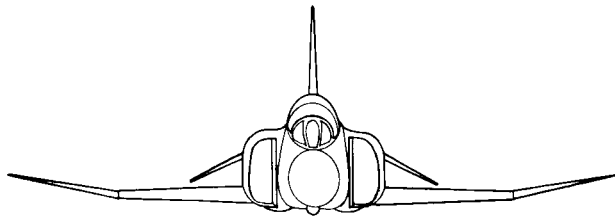
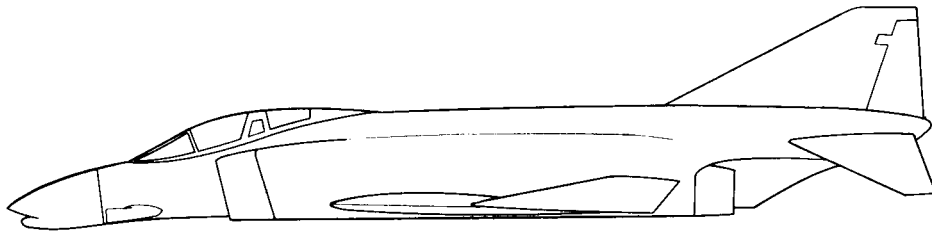
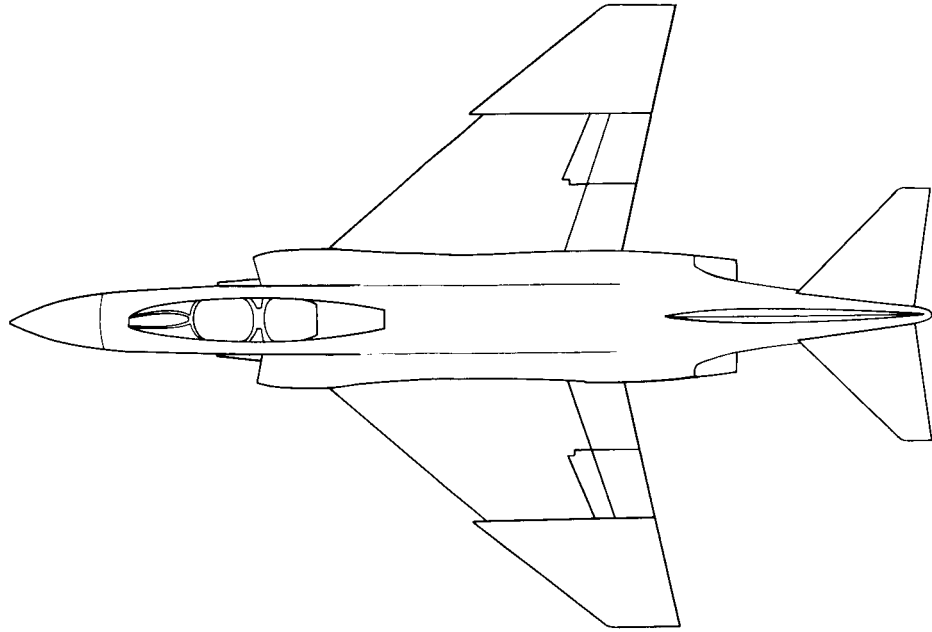
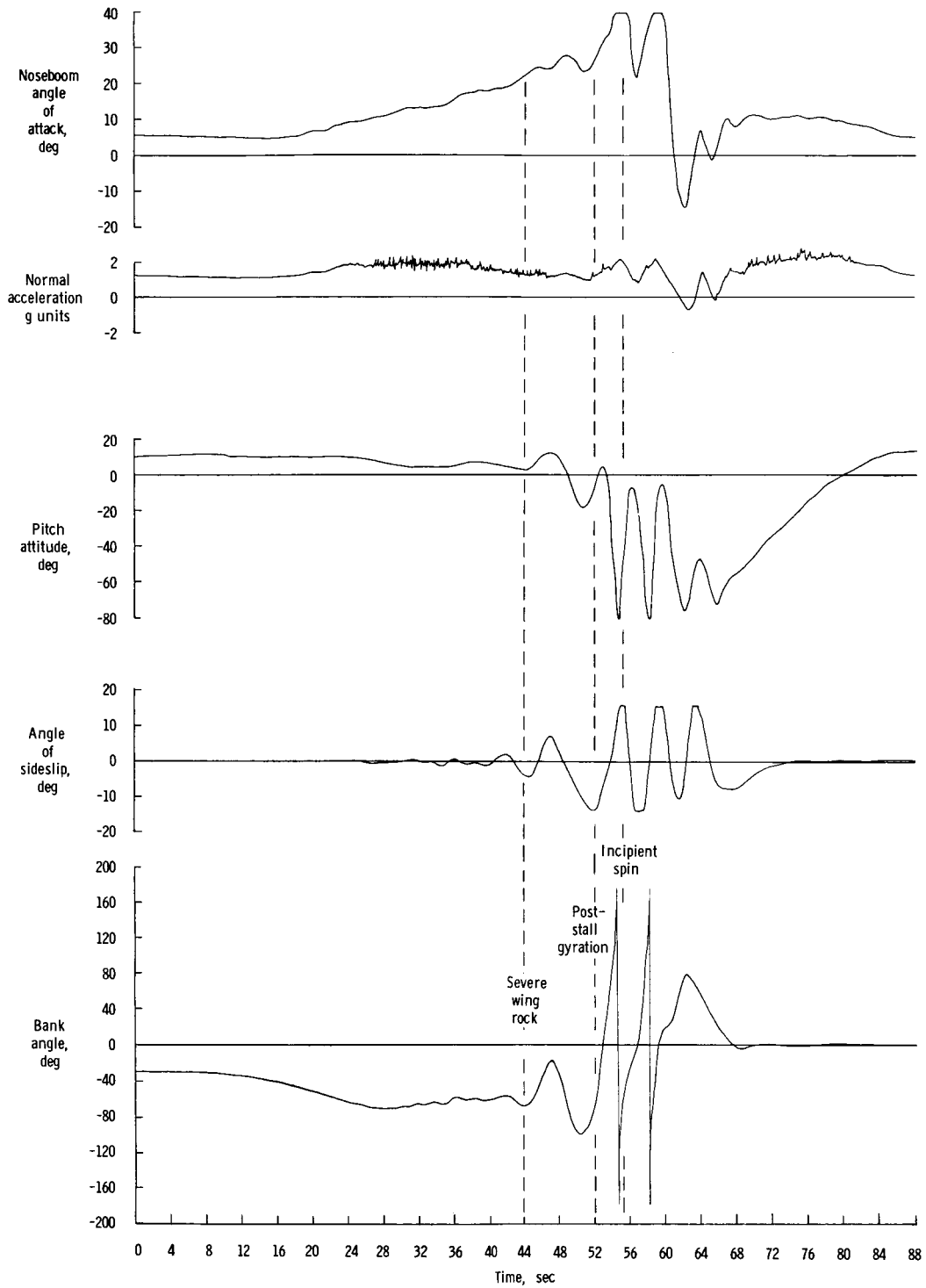
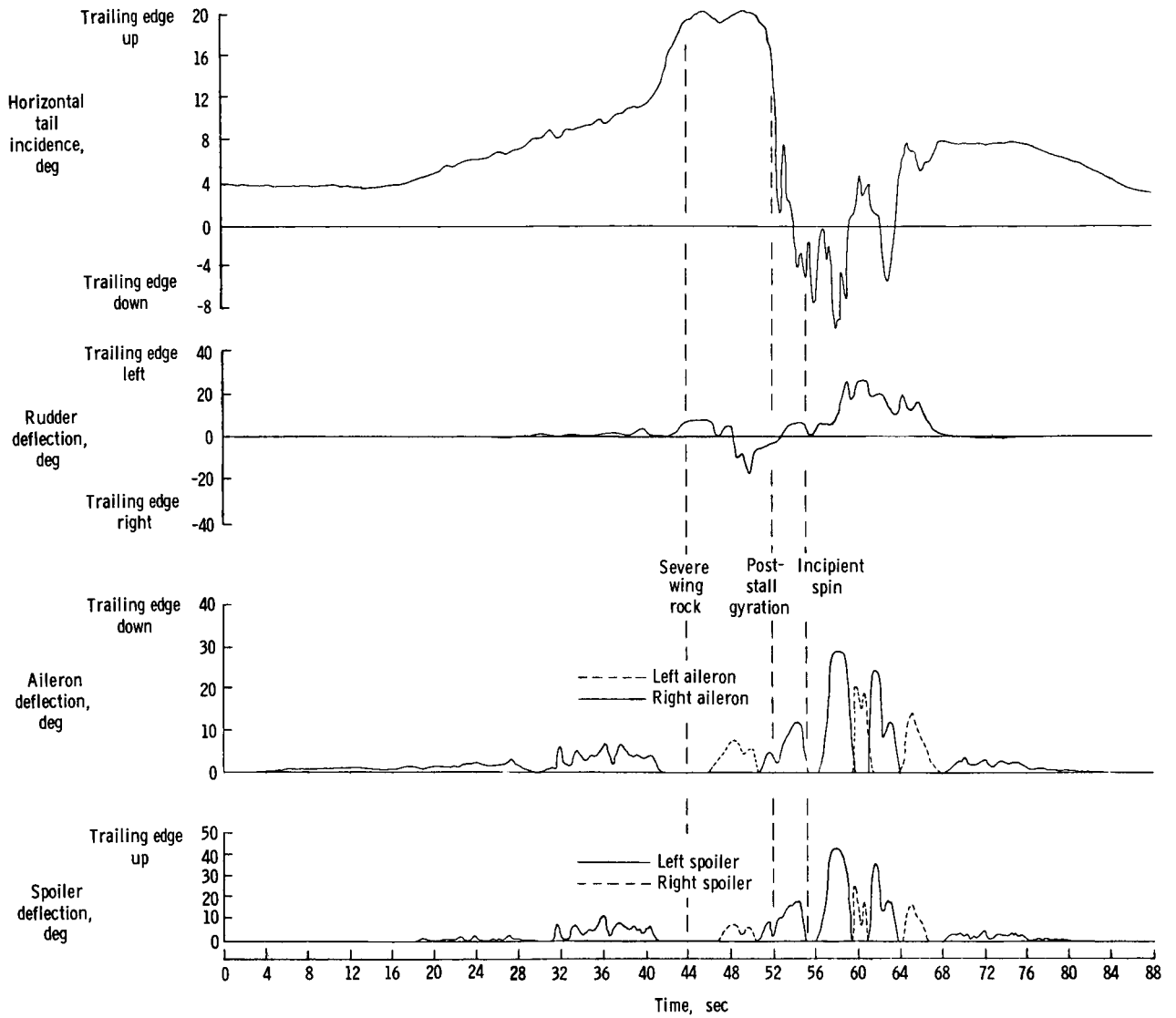


Figure 1.- Three-view sketch of airplane configuration.



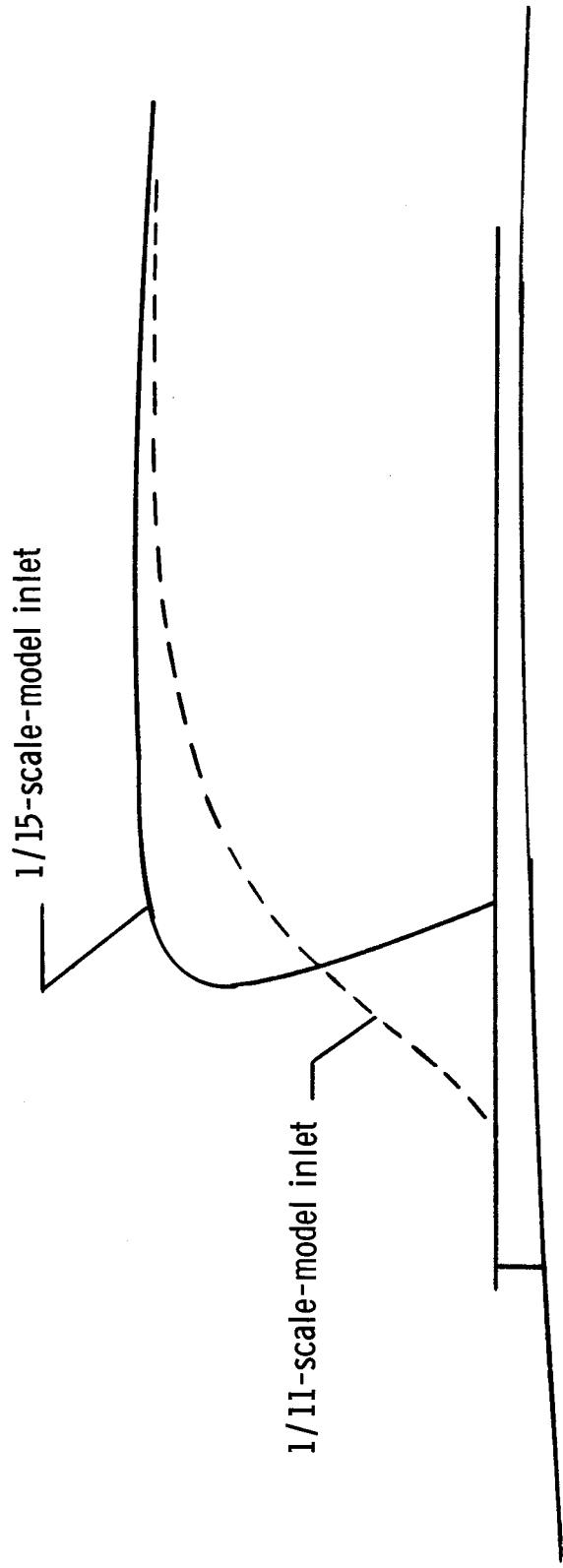
(a) Flight variables.

Figure 2.- Time histories of directional divergence encountered in flight.

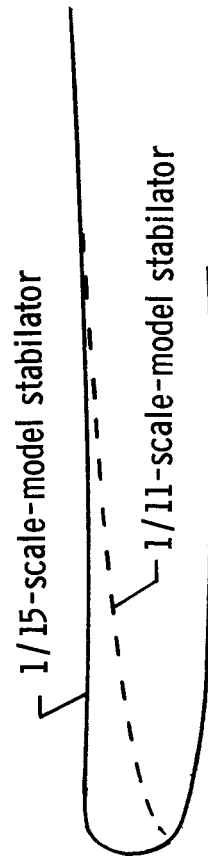


(b) Control-surface deflections.

Figure 2.- Concluded.

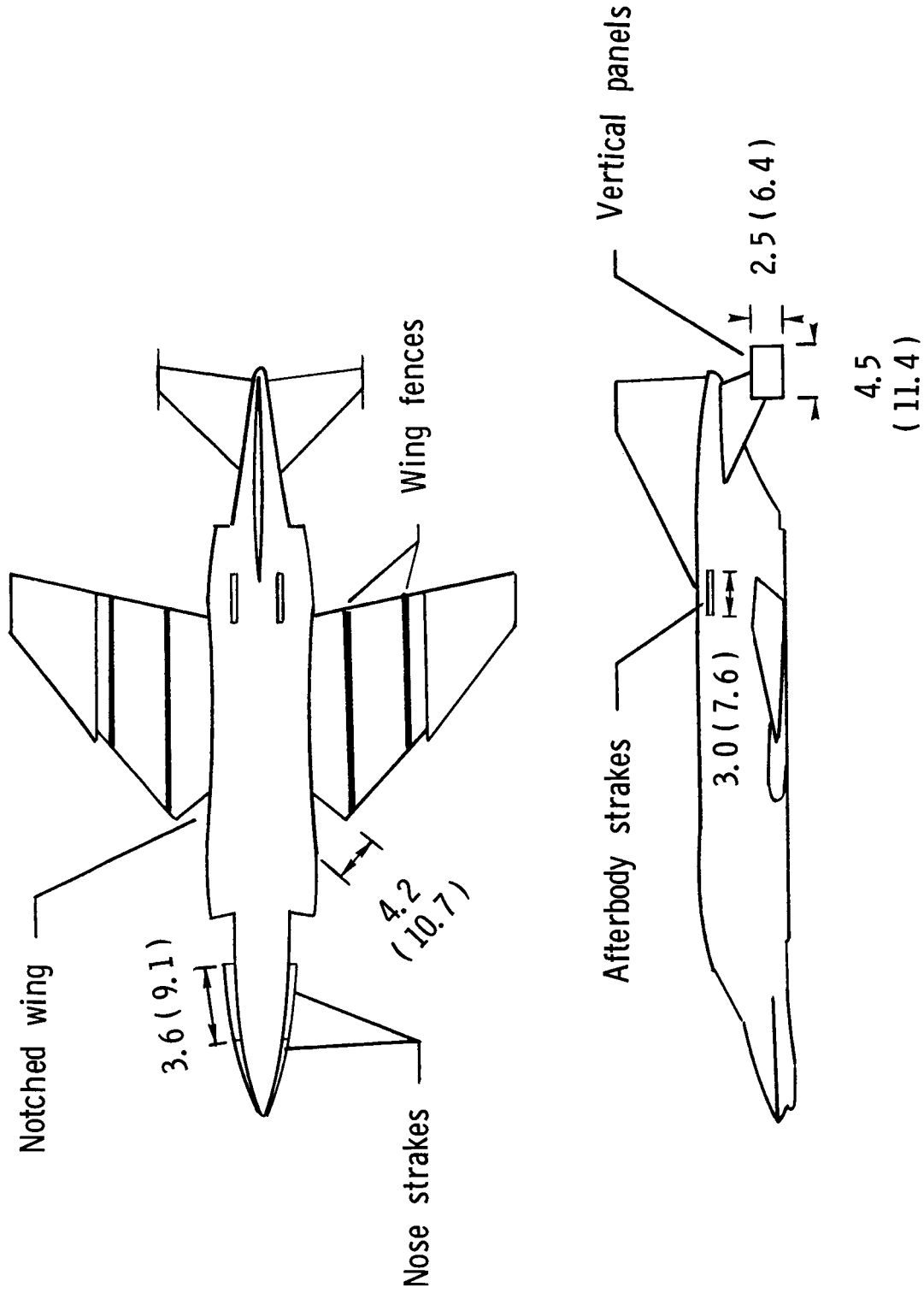


(a) Plan view of engine inlets.



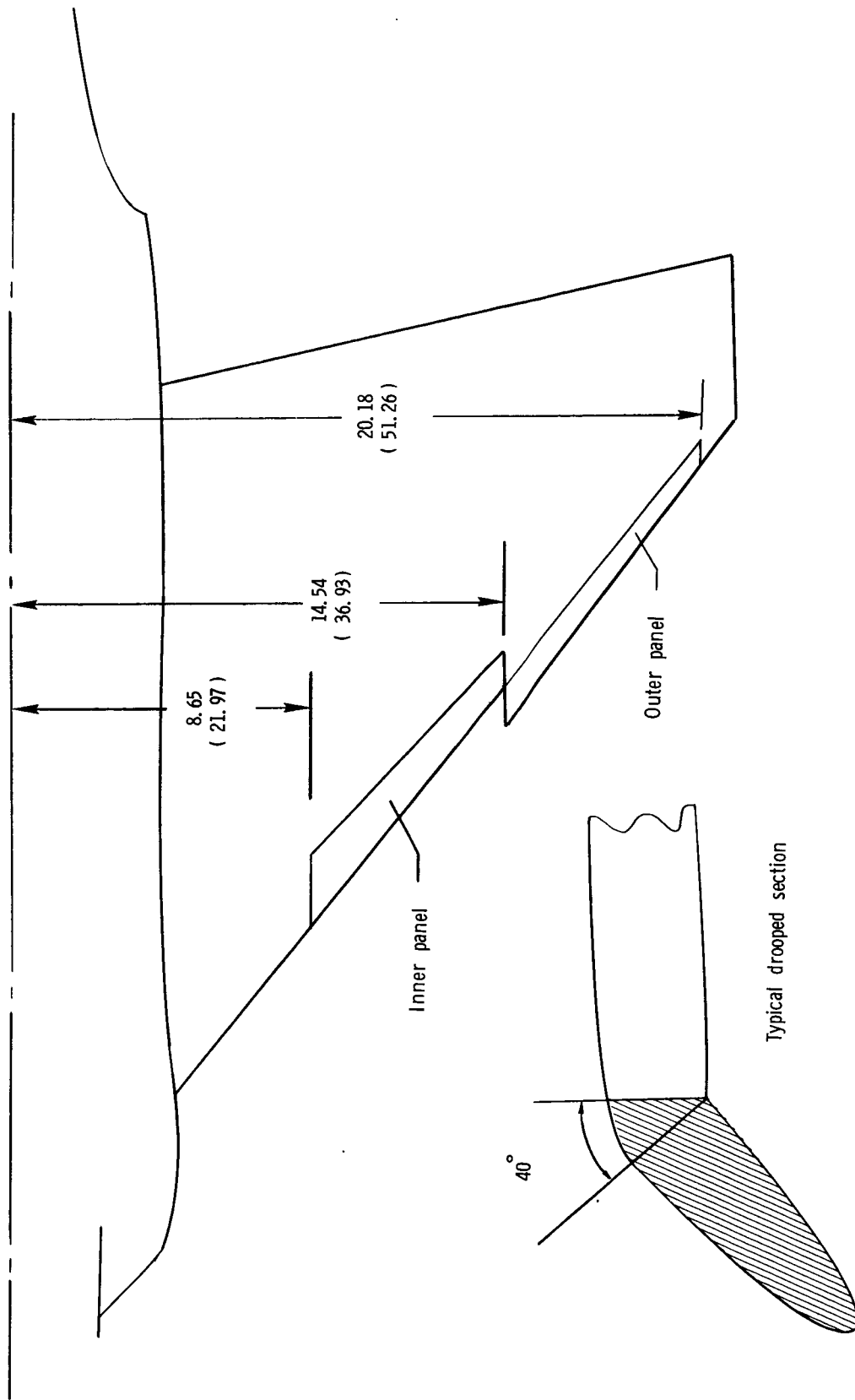
(b) Stabilizer leading edge.

Figure 3.- Sketches of geometric differences between models.



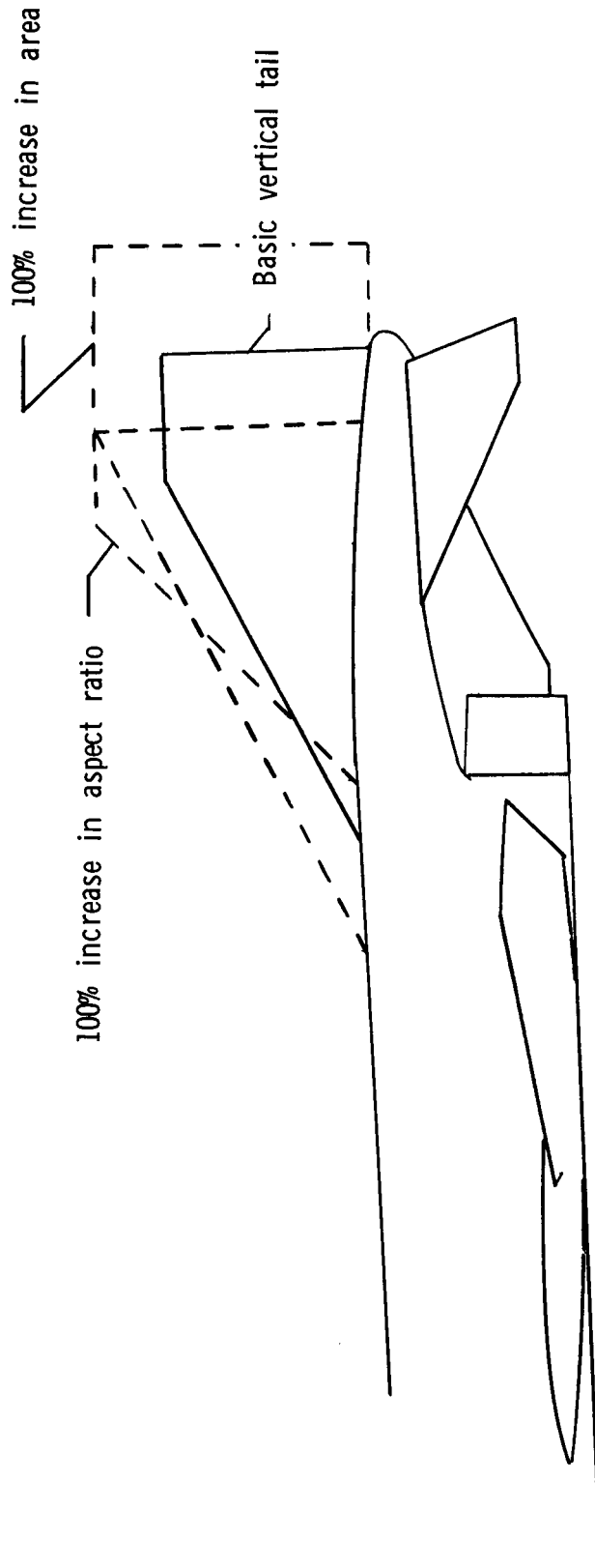
(a) Strakes, wing apex notch, wing fences, and tip tails.

Figure 4.- Airframe modifications tested on 1/11-scale model. Dimensions are in inches (cm).



(b) Leading-edge droop.

Figure 4.- Continued.



Note: Vertical tail length l_v constant

(c) Vertical tail modifications.

Figure 4.- Concluded.

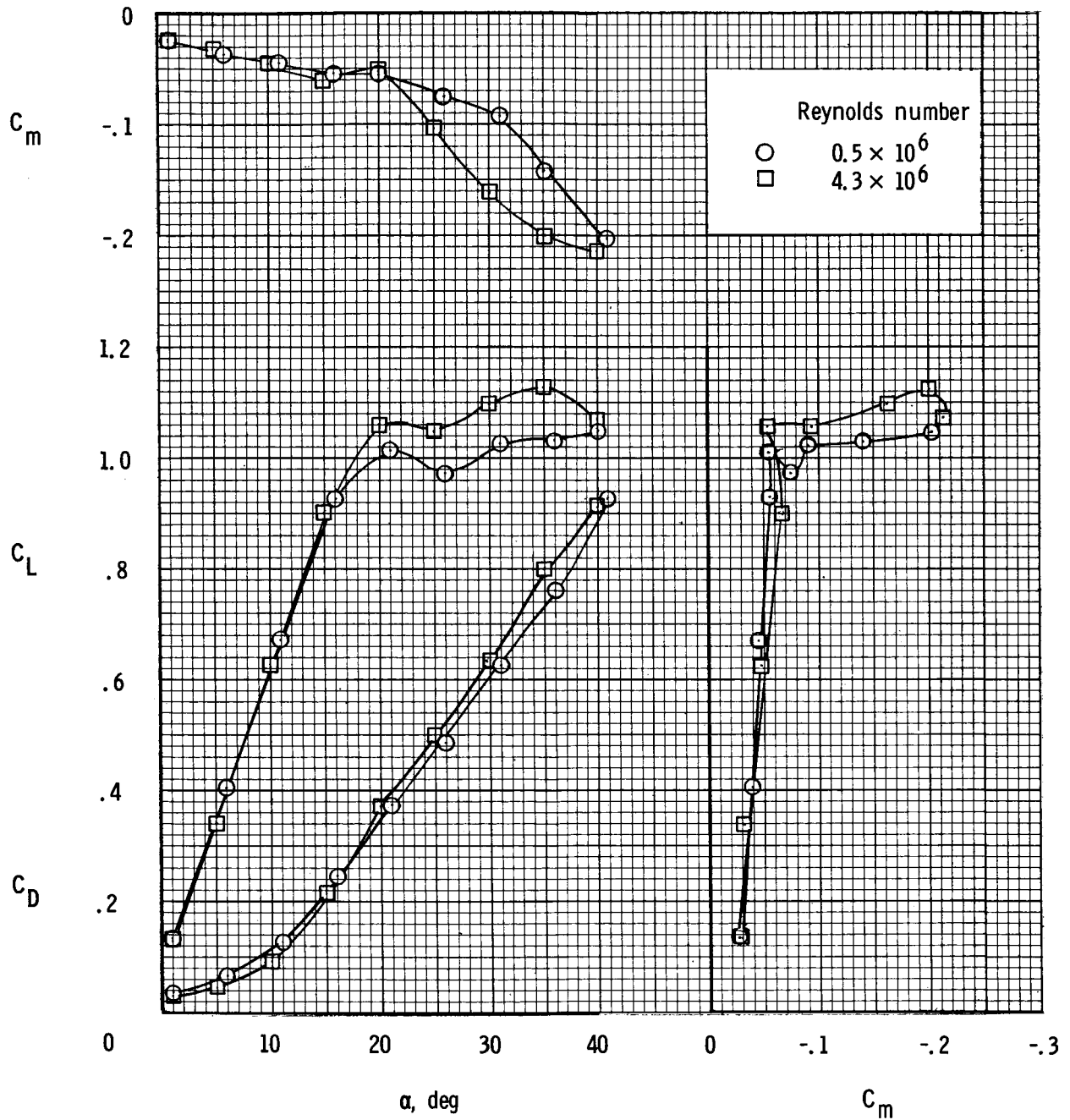


Figure 5.- Variation of static longitudinal characteristics with angle of attack. $i_t = 0^\circ$.

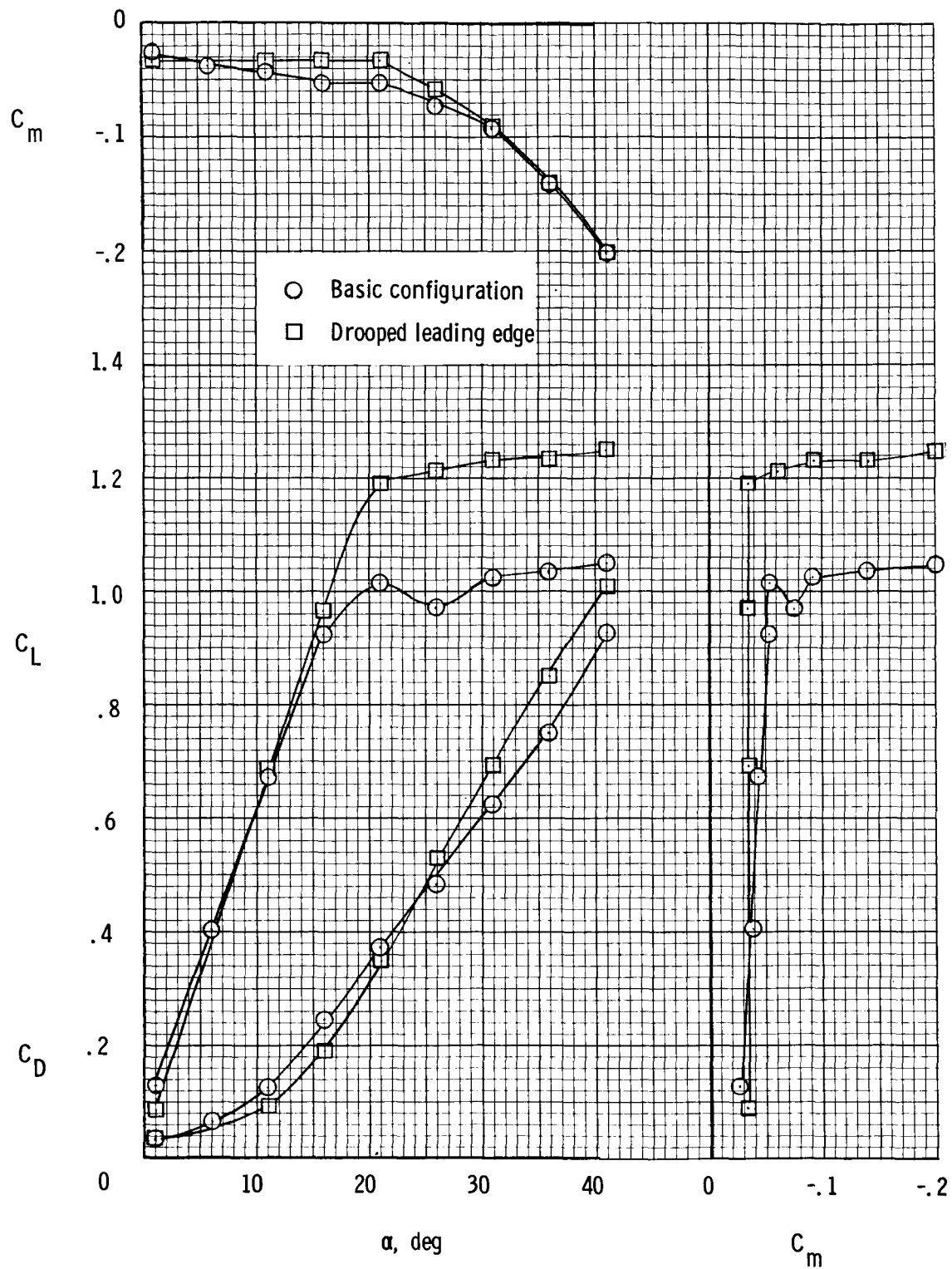


Figure 6.- Effect of wing leading-edge droop on longitudinal characteristics. $i_t = 0^\circ$.

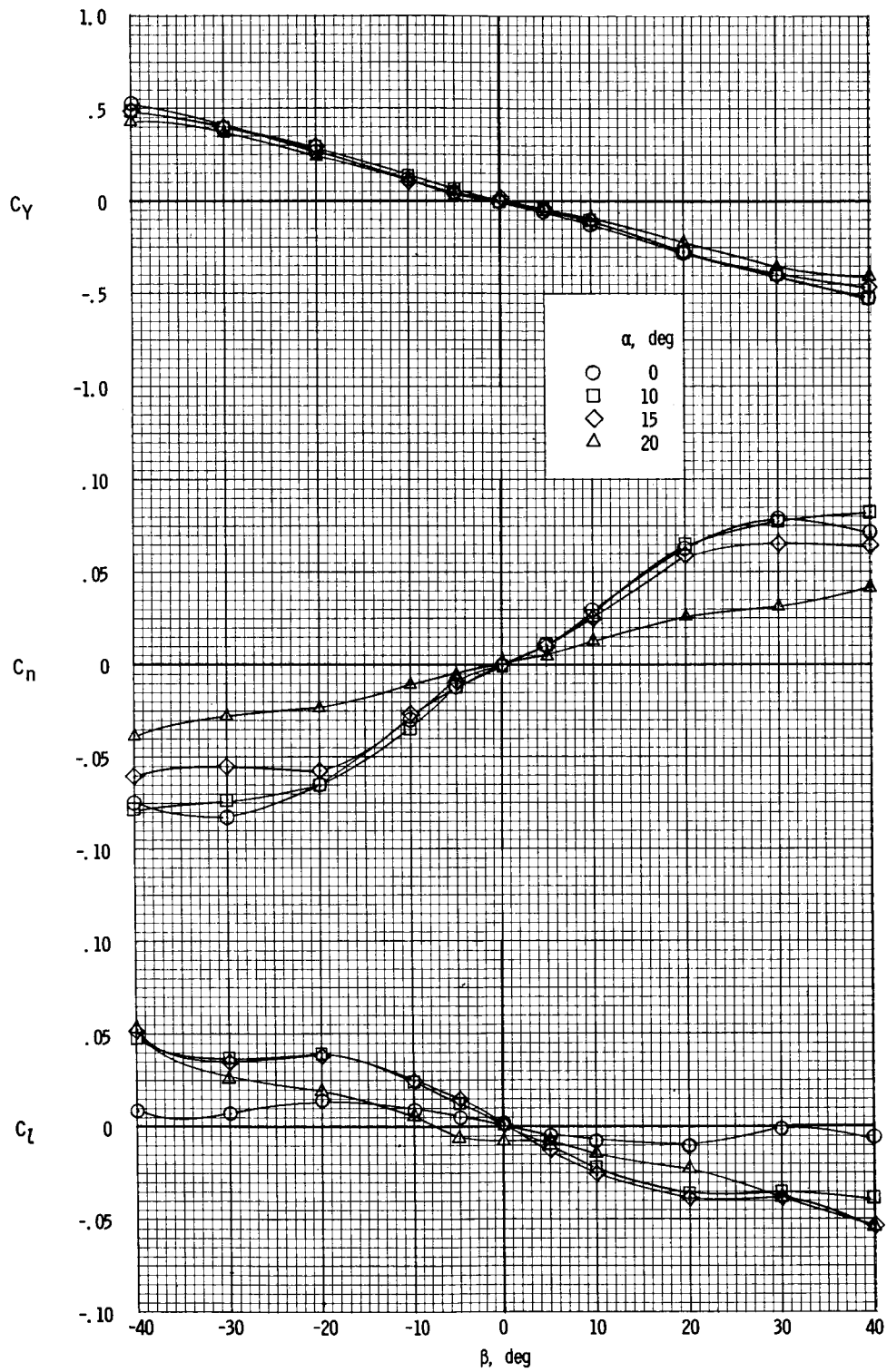


Figure 7.- Variation of static lateral-directional characteristics with angle of sideslip.

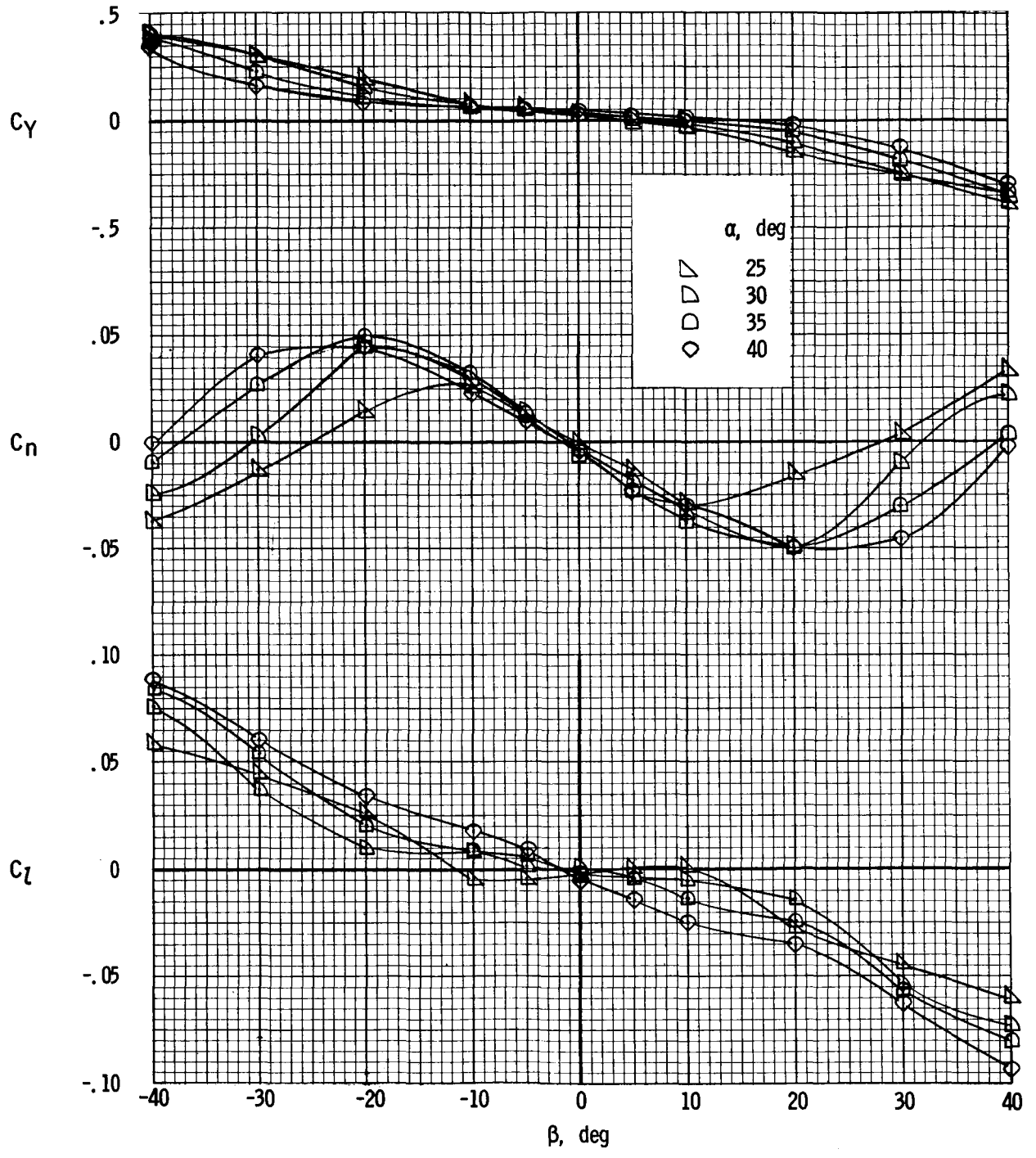


Figure 7.- Concluded.

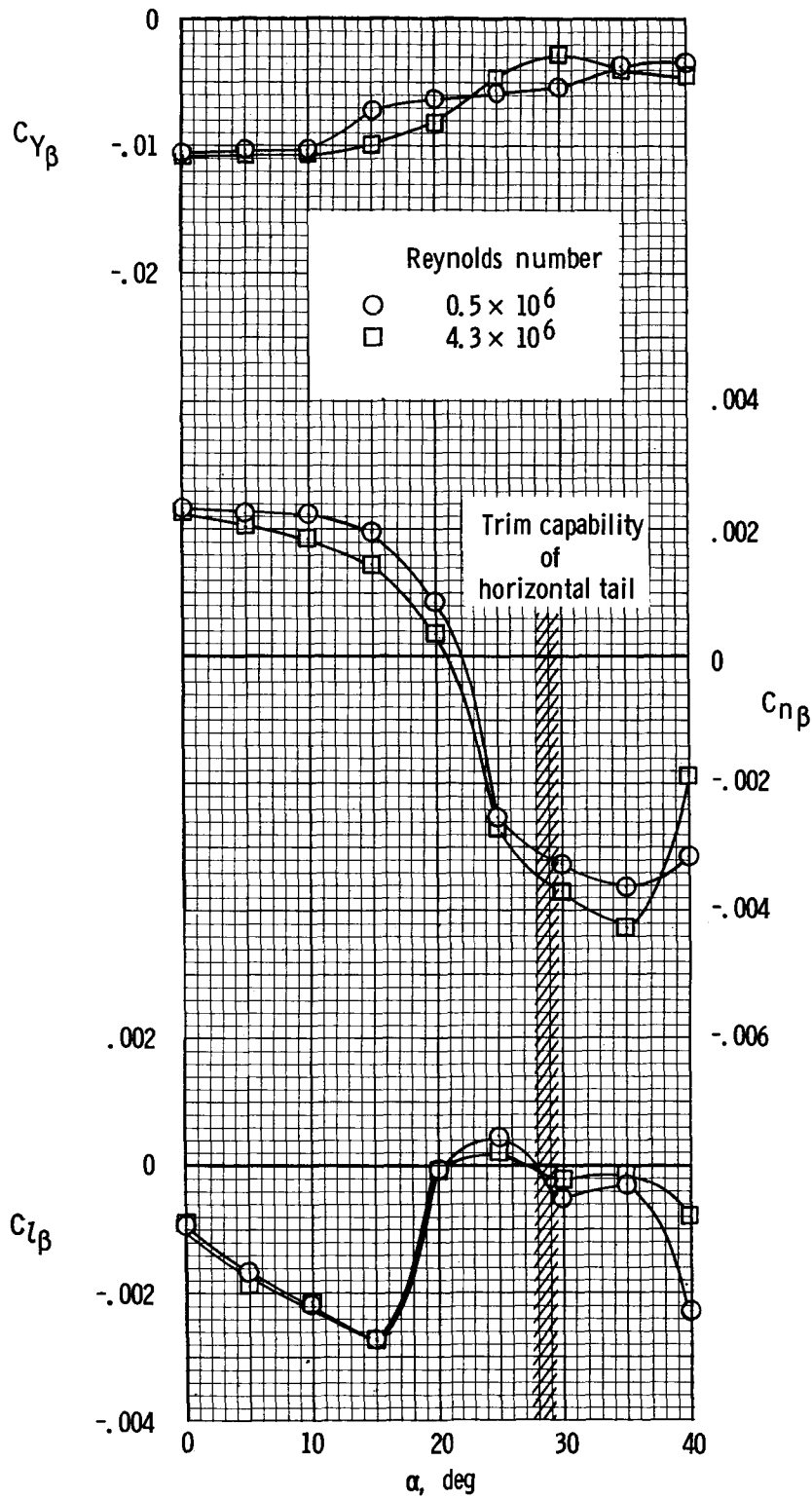
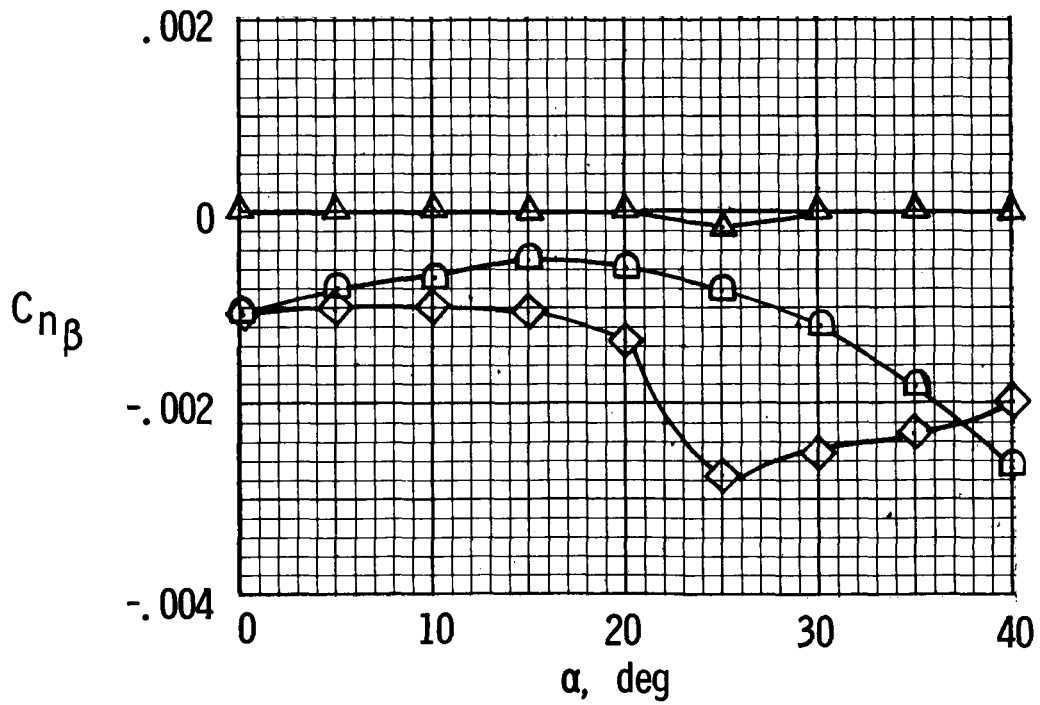
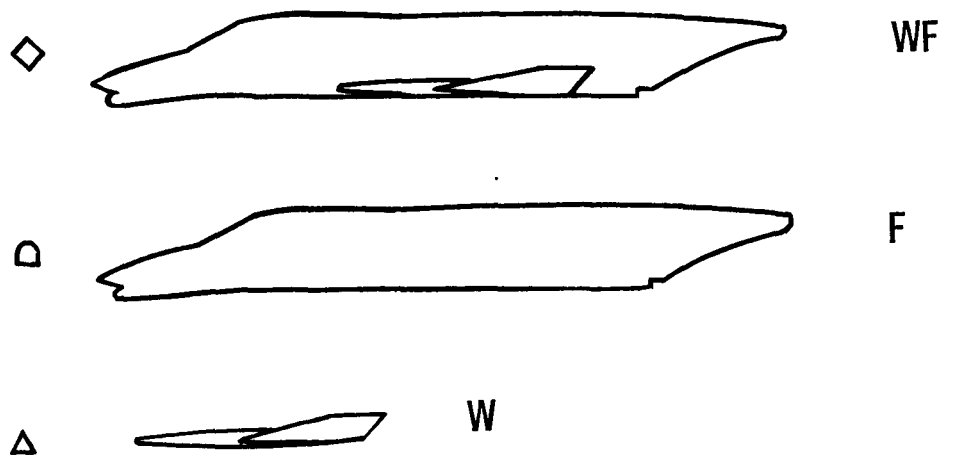
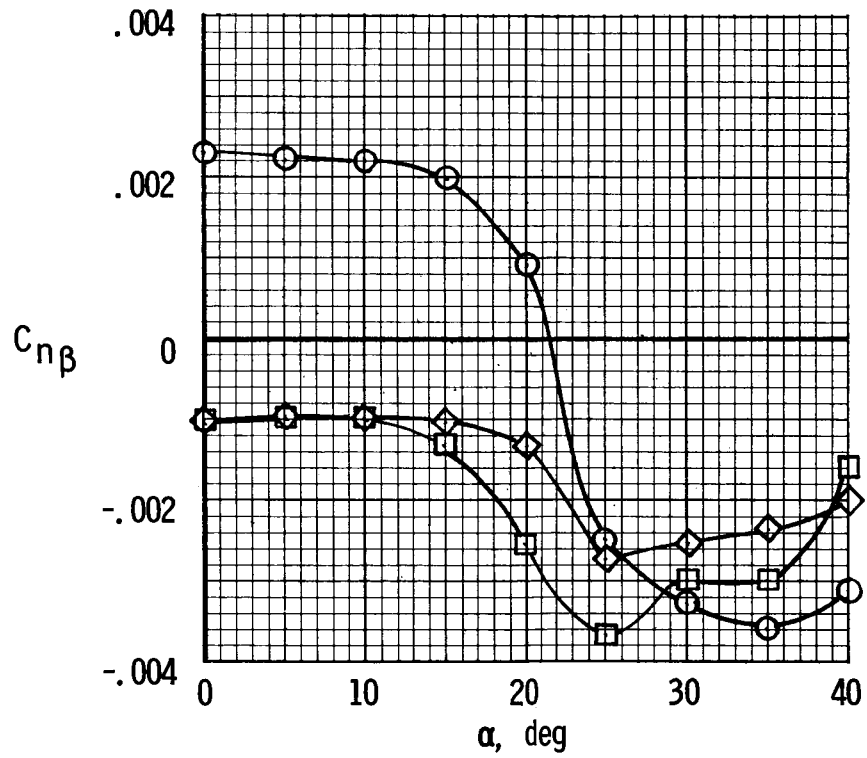
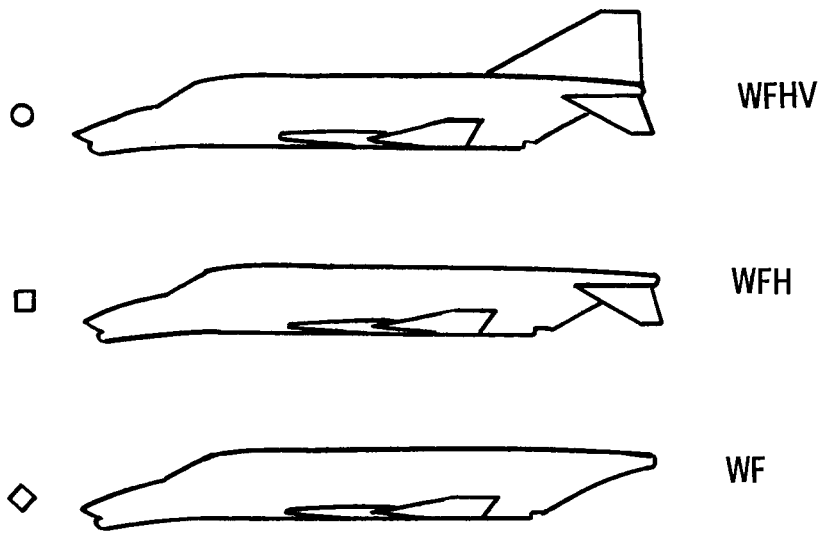


Figure 8.- Variation of static lateral-directional stability derivatives with angle of attack.



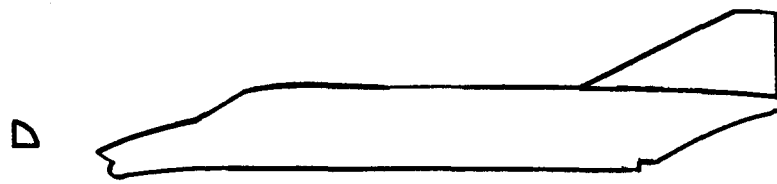
(a) Wing and fuselage characteristics.

Figure 9.- Effect of various airframe components on $C_{n\beta}$.

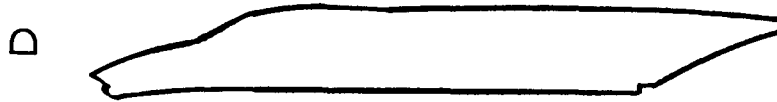


(b) Vertical and horizontal tail characteristics.

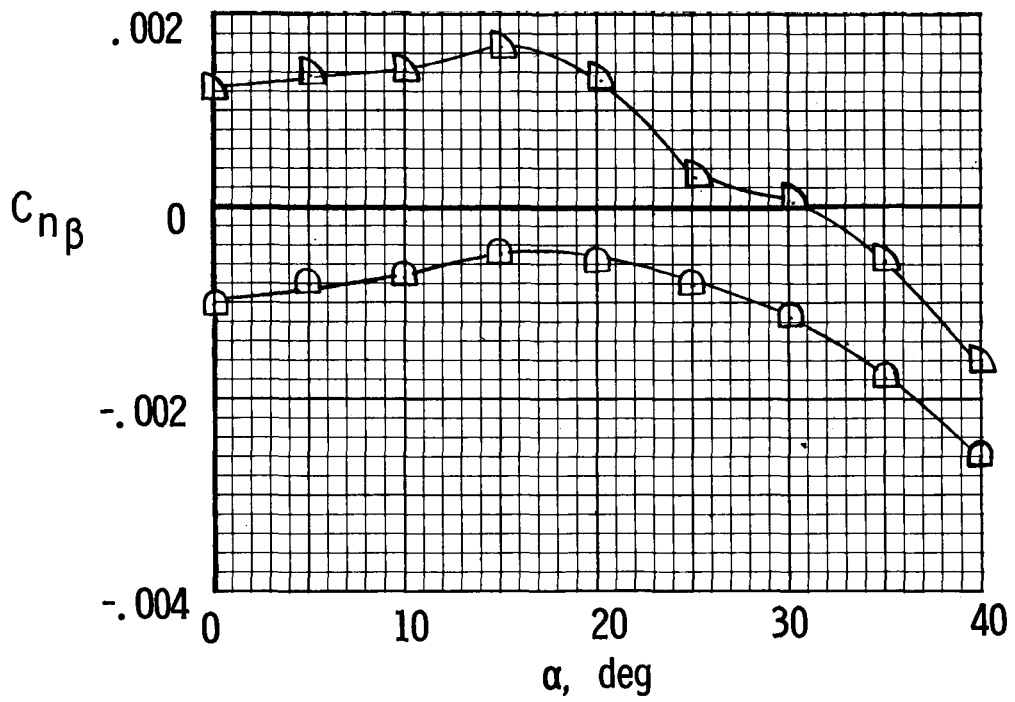
Figure 9.- Continued.



FV

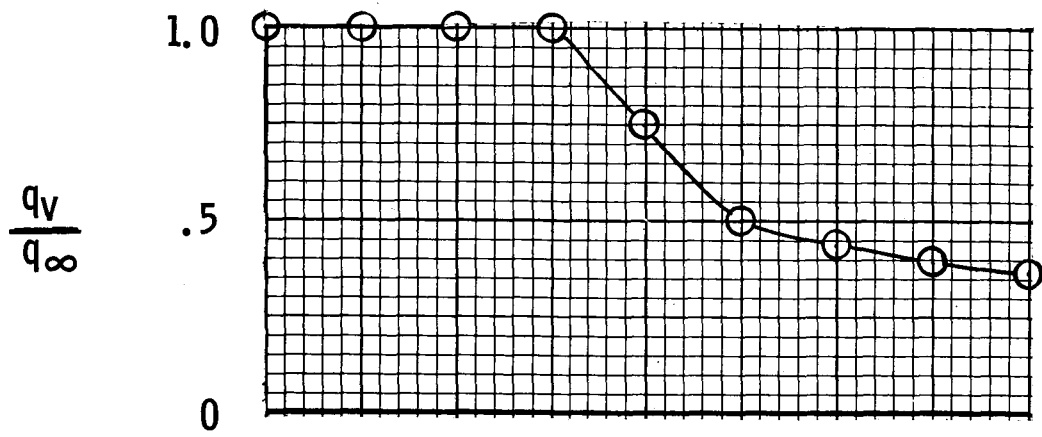


F

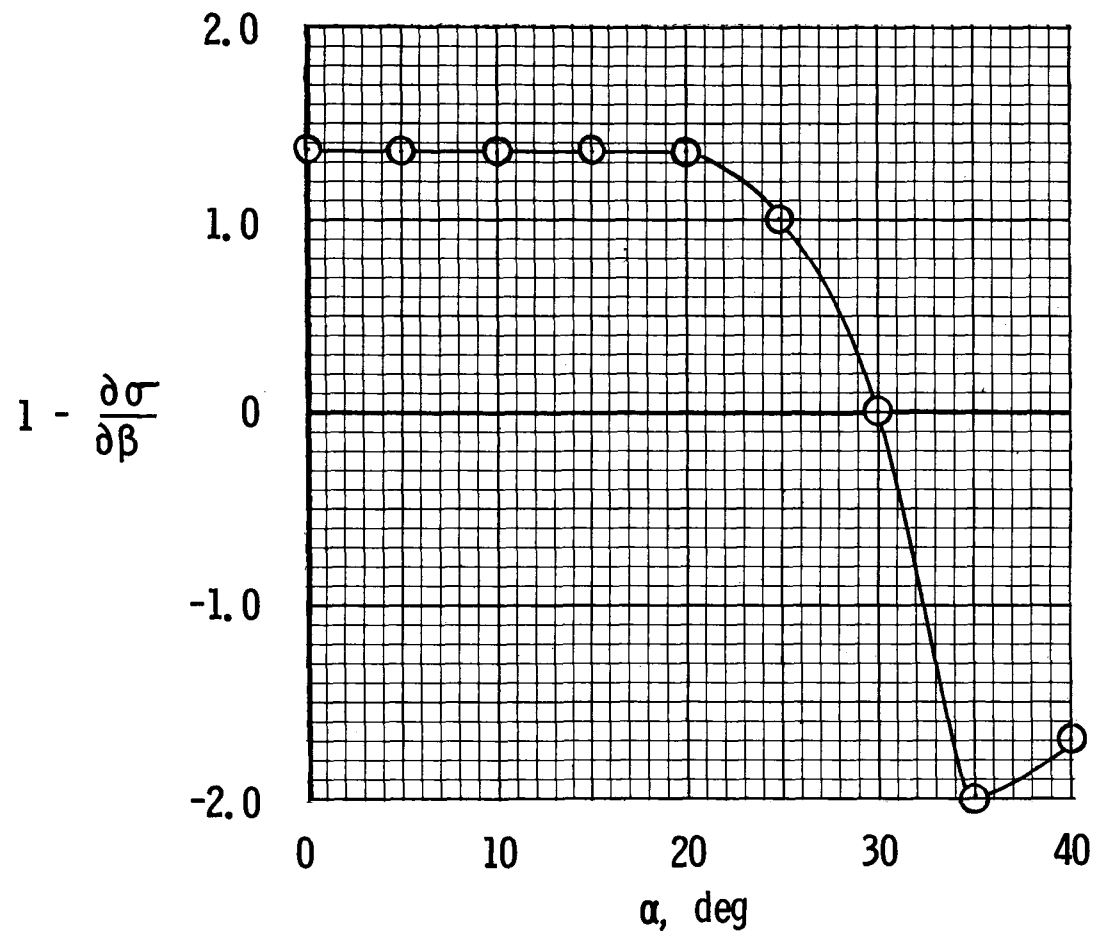


(c) Fuselage and vertical tail characteristics.

Figure 9.- Concluded.



(a) Dynamic-pressure ratio.



(b) Sidewash parameter.

Figure 10.- Variation with angle of attack of parameters affecting vertical tail effectiveness.

- Basic vertical tail
- △ Aspect ratio increased 100%
- ◇ Area increased 100%
- Vertical tail off

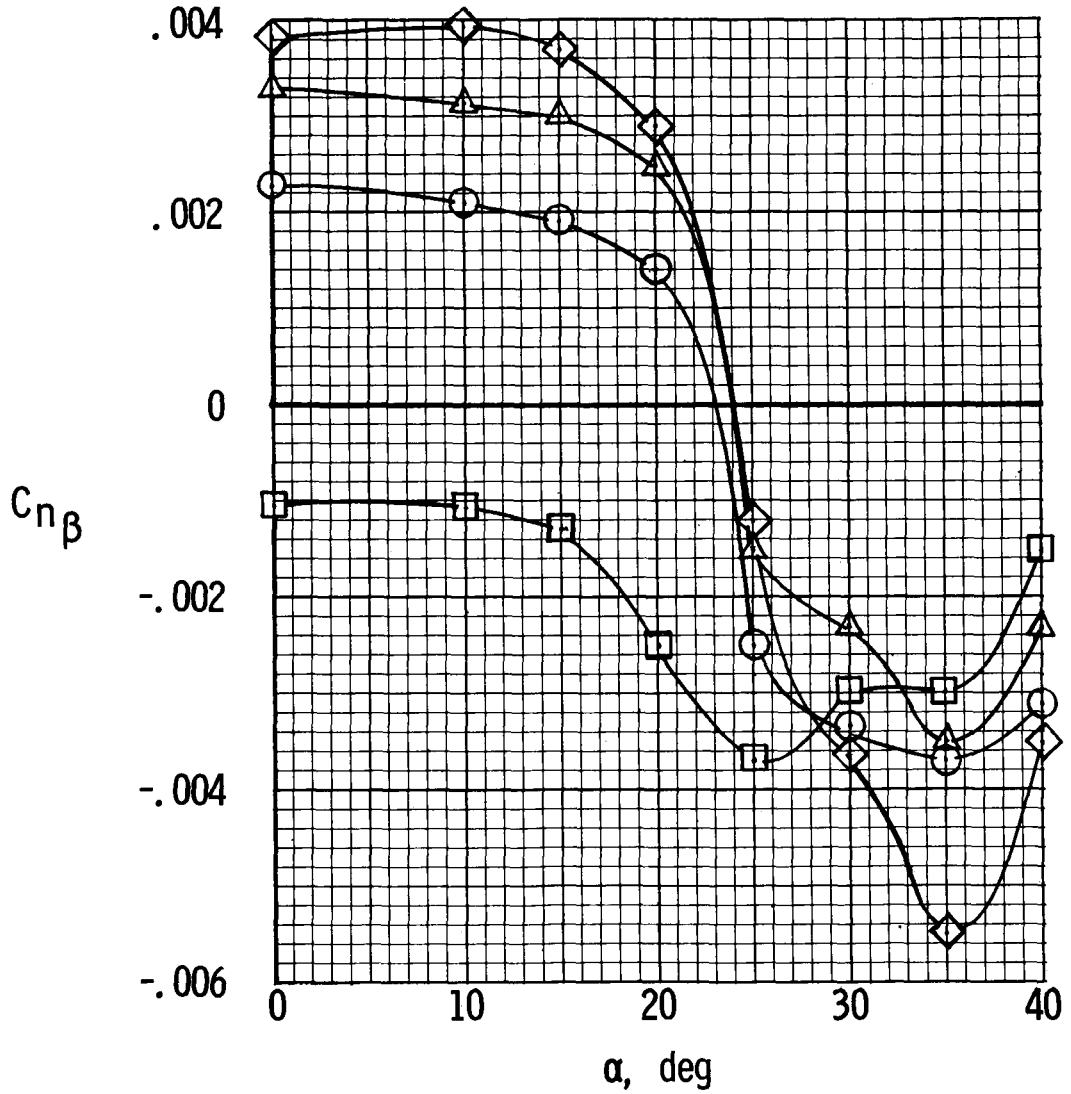


Figure 11.- Effect of vertical tail modifications on $C_{n\beta}$.

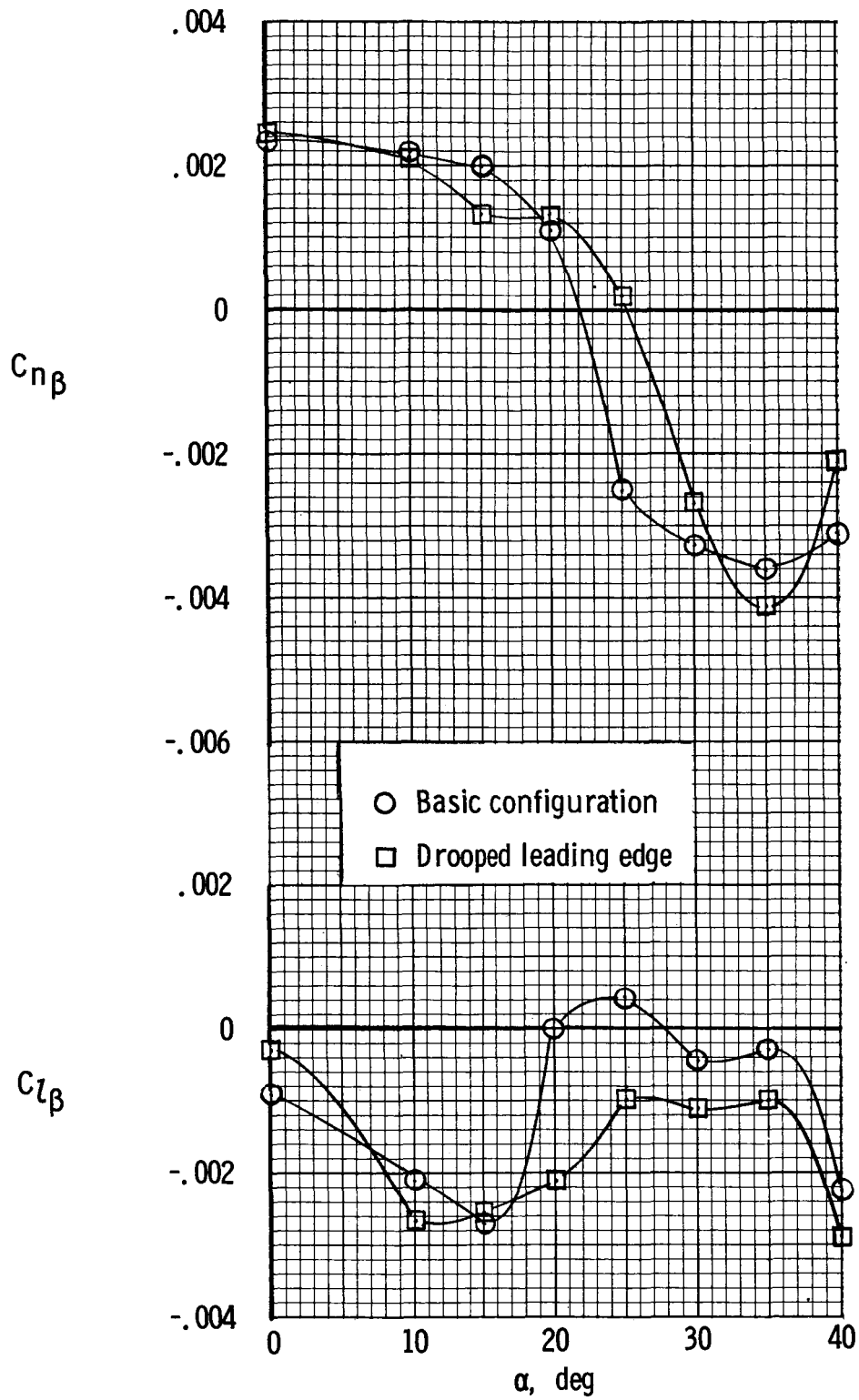
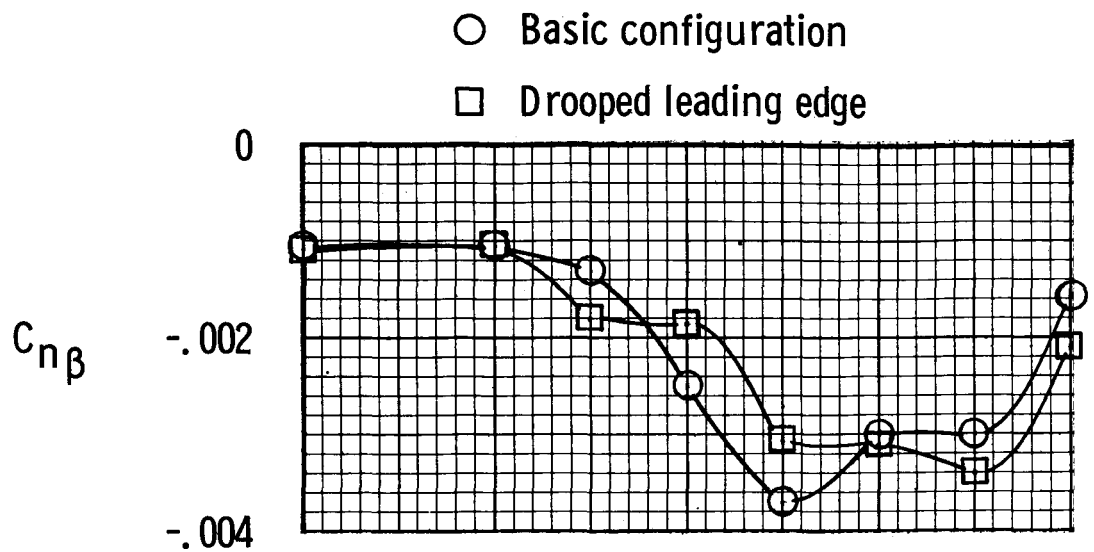
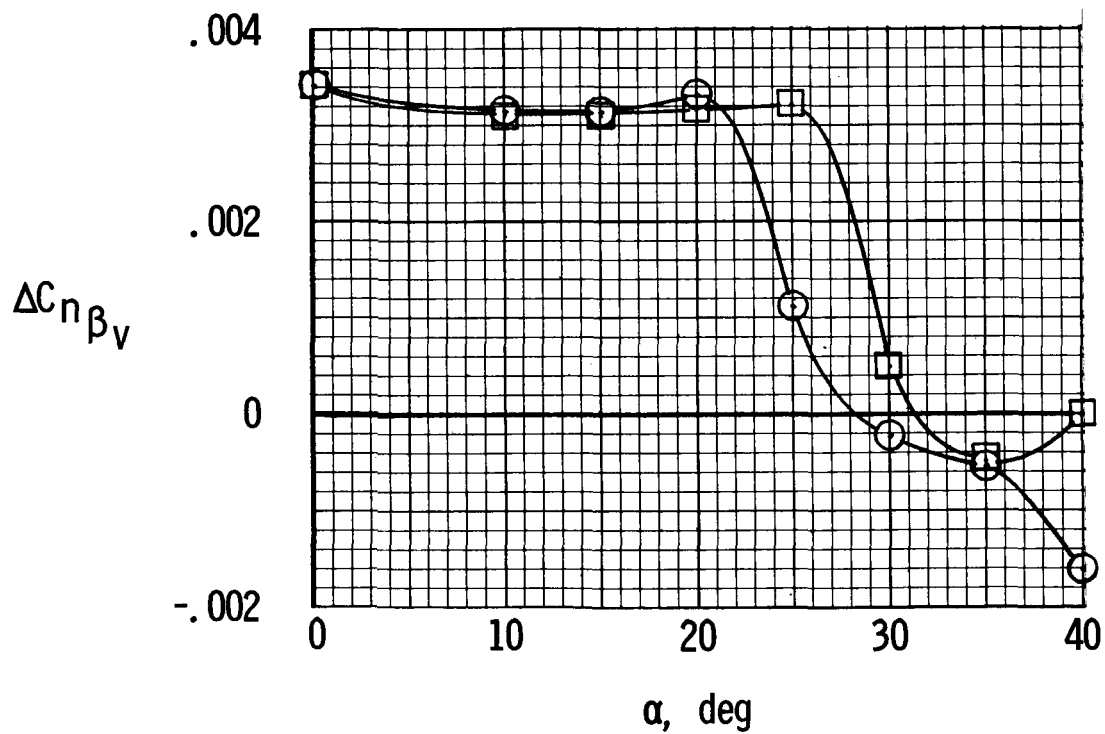


Figure 12.- Effect of wing leading-edge droop on $C_{n\beta}$ and $C_{l\beta}$. Inner and outer panels drooped.



(a) Vertical tail off.



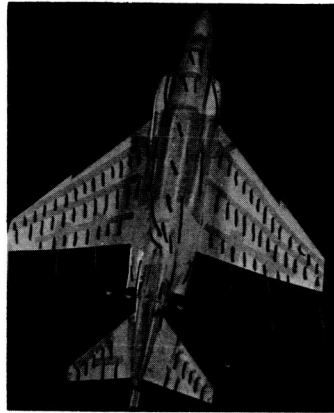
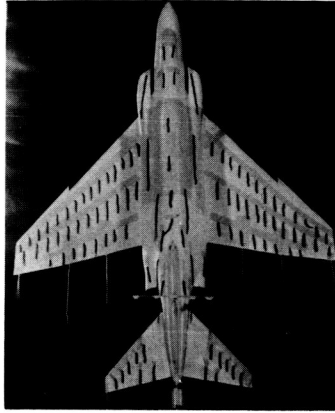
(b) Vertical tail contribution.

Figure 13.- Effect of wing leading-edge droop on directional stability characteristics.

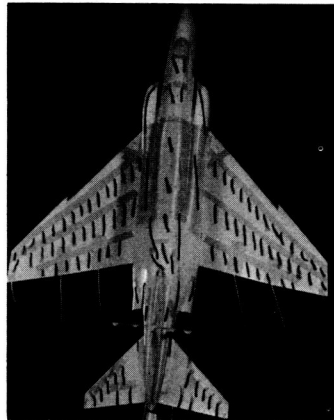
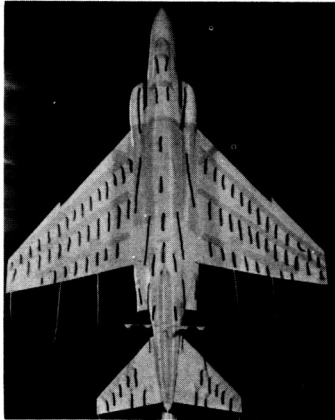
$\beta = 0^\circ$

$\beta = -10^\circ$

$\alpha = 0^\circ$



$\alpha = 5^\circ$



$\alpha = 10^\circ$

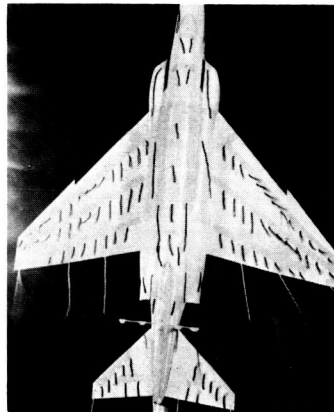
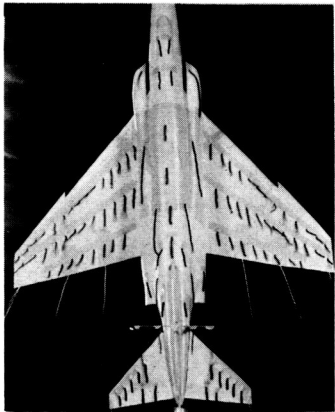


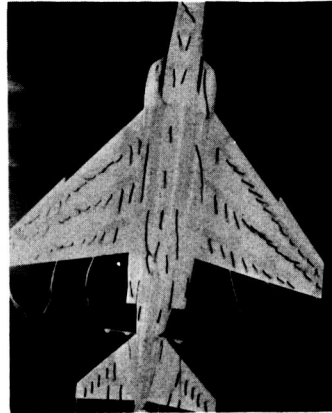
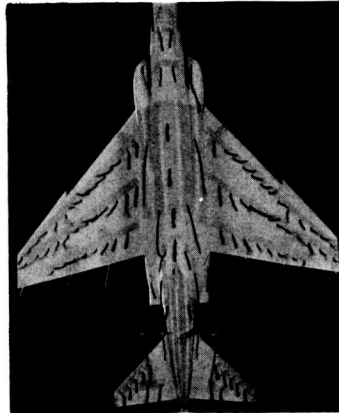
Figure 14.- Photographs of tuft studies at various values of angle of attack for $\beta = 0^\circ$ and $\beta = -10^\circ$.

L-69-1398

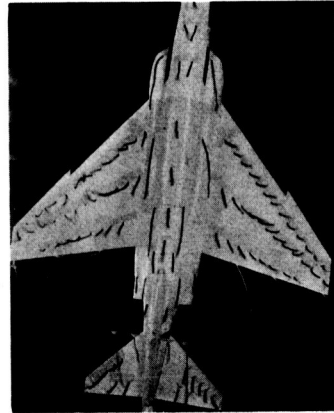
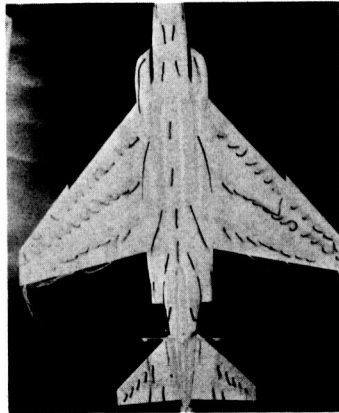
$\beta = 0^\circ$

$\beta = -10^\circ$

$\alpha = 15^\circ$



$\alpha = 20^\circ$



$\alpha = 25^\circ$

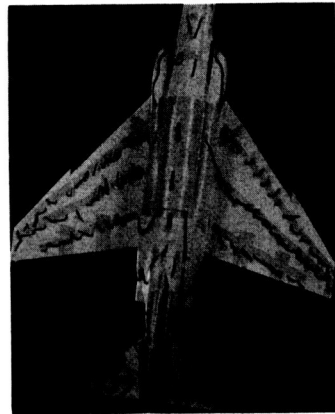
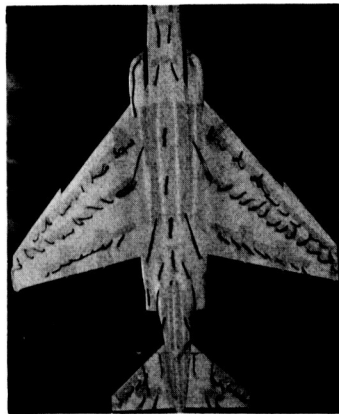


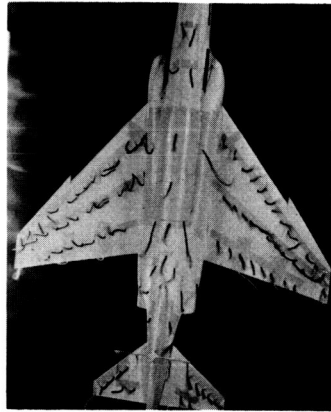
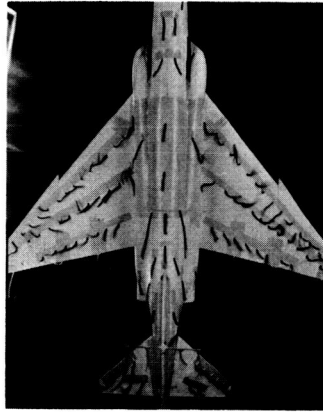
Figure 14.- Continued.

L-69-1399

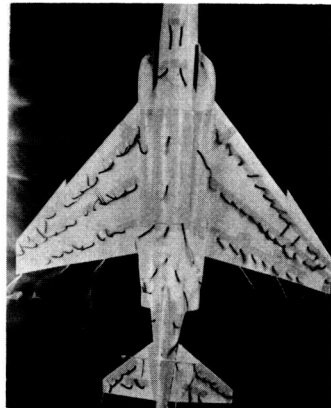
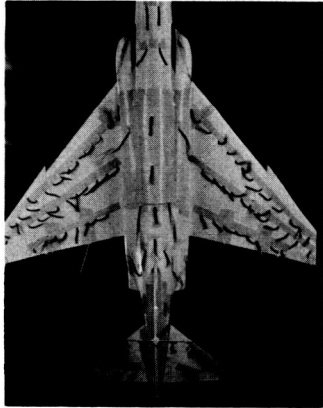
$\beta = 0^\circ$

$\beta = -10^\circ$

$\alpha = 30^\circ$



$\alpha = 35^\circ$



$\alpha = 40^\circ$

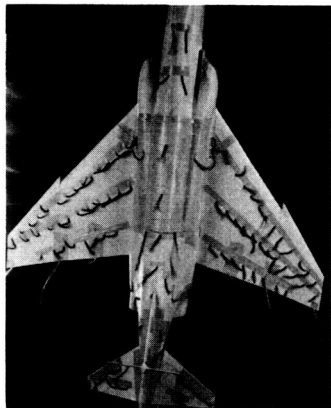
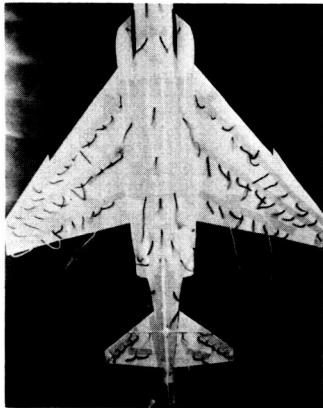
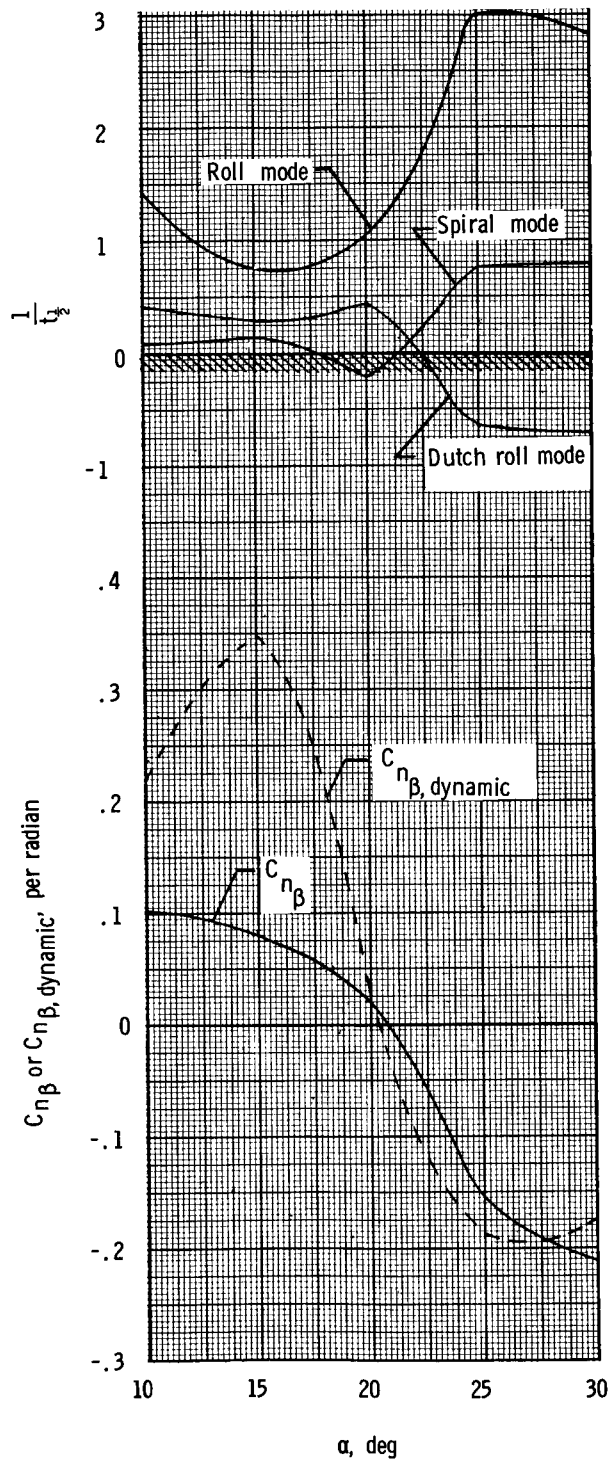


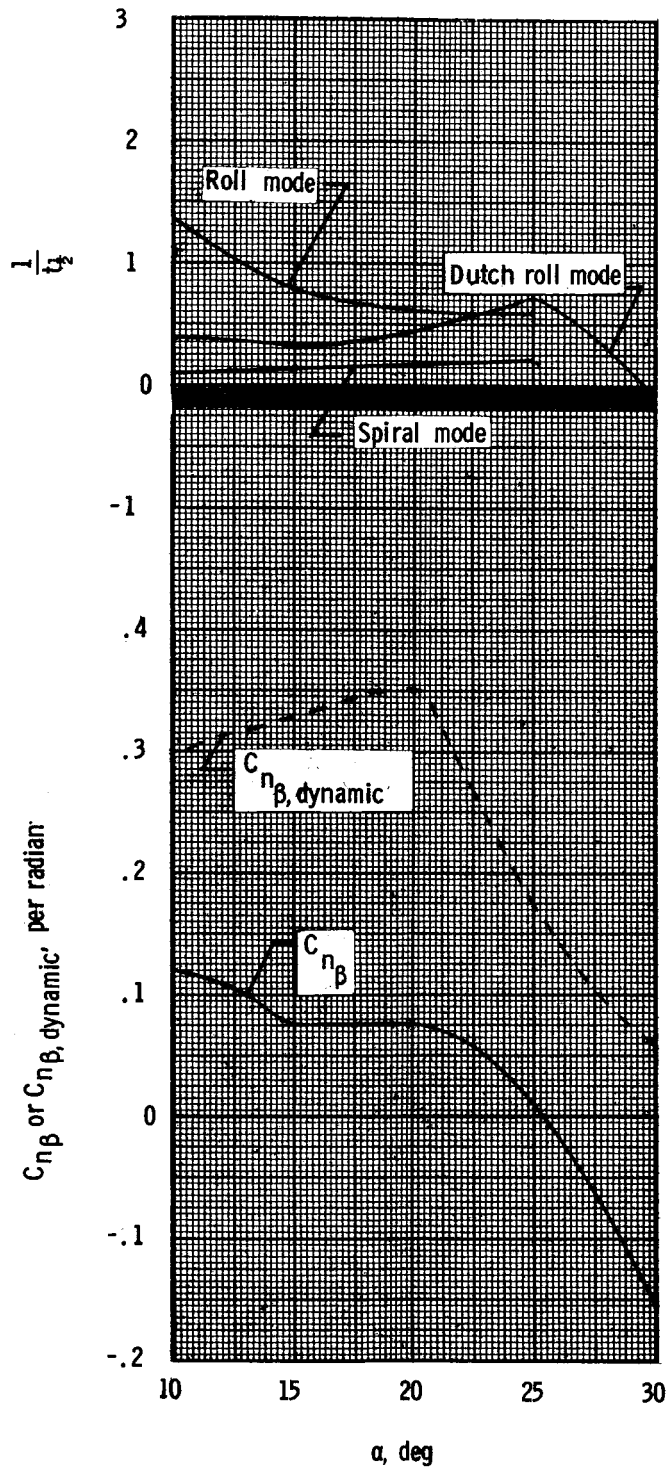
Figure 14.- Concluded.

L-69-1400



(a) Basic configuration.

Figure 15.- Results of dynamic stability calculations.



(b) Modified configuration.

Figure 15.- Concluded.